Robin-Robin loose coupling for incompressible fluid-structure interaction: non-linear setting and nearly-optimal error analysis

Erik Burman, Rebecca Durst, Miguel Angel Fernández, Johnny Guzmán, Oscar Ruz

ROBIN-ROBIN LOOSE COUPLING FOR INCOMPRESSIBLE FLUID-STRUCTURE INTERACTION: NON-LINEAR SETTING AND NEARLY-OPTIMAL ERROR ANALYSIS*

ERIK BURMAN†, REBECCA DURST‡, MIGUEL A. FERNÁNDEZ§, JOHNNY GUZMÁN‡, AND OSCAR RUZ§

Abstract. The numerical simulation of incompressible fluid-structure interaction systems with loosely coupled schemes is a delicate problem. Indeed, the splitting method must both be stable for the full nonlinear system and have sufficient accuracy to be of use in practice. In the case of the coupling of an incompressible fluid with thick-walled solids the error analyses reported in the literature are limited to $\mathcal{O}(\tau^{\frac{1}{2}})$ accuracy in time, where τ denotes the time step. The objective of the present work is to show two important extensions of the analysis of the Robin-Robin loosely coupled scheme recently reported in *[Numer. Math., 151(4):807–840, 2022]*. First, we give a formulation of the scheme in a general non-linear setting and prove its unconditional energy stability. Then we show that nearly-optimal $\mathcal{O}\big(\tau\sqrt{1+\log\tau^{-1}}\big)$ accuracy can be achieved in the linear case. These theoretical findings are illustrated in a series of numerical examples.

Key words. Fluid-structure interaction, loosely coupled scheme, moving domains, Robin conditions, optimal accuracy

MSC codes. 74F10, 65M12, 76M10

1. Introduction.

The numerical approximation of the interaction of an elastic solid with an incompressible viscous fluid over a moving interface (FSI) remains a challenging problem in scientific computing. For a global overview of the framework and different approaches with special focus on cardiovascular flow which is a relevant application for the discussion herein, we refer to [16, 19]. Typically the problem is nonlinear both through the separate subproblems and the moving interface. The coupling is very stiff due to the different time scales of the subproblems. In particular, the incompressibility and the related compatibility conditions present difficulties. For computational efficiency it is appealing to use a loosely coupled scheme to advance the coupled problem in time. In such an approach one solve is performed in each subdomain and the coupling data is tranferred across the interface in a staggered manner. Although this is feasible in elasto-acoustic, where the fluid is compressible (see, e.g., [15]), it is much more delicate in the incompressible regime due to the added-mass effect (see [12, 20]) unless special care is taken in the design of the coupling conditions.

The first stable loosely coupled scheme for FSI in the presence of incompressibility was proposed in [9], using Nitsche's method for FSI (see [24]) in combination with a pressure stabilization that relaxes the incompressibility on the interface. For this type of method, however, the stiffness of the Nitsche penalty term introduces the parabolic condition $\tau \lesssim h^2$ for overall first-order accuracy (but not for stability), where τ stands for the time-step length and h for the spatial grid parameter. It was then noted in

*Submitted to the editors DATE.

Funding: Supported by the French National Research Agency (ANR) through the SIMR project (ANR-19-CE45-0020), and by Inria through the IMFIBIO associated team.

†Department of Mathematics, University College London, London, United Kingdom (e.burman@ucl.ac.uk).

‡Division of Applied Mathematics, Brown University, Providence, USA (rebecca_durst@alumni.brown.edu,johnny_guzman@brown.edu).

§Sorbonne Université, Inria & CNRS, UMR 7598, Laboratoire Jacques-Louis Lions, Paris, France (miguel.fernandez@inria.fr,oscar.ruz@inria.fr).

[10] that the Nitsche coupling method could be transformed into Robin type coupling scheme without loss of stability. Robin conditions had been shown to perform well as a preconditioner already in [1]. A number of studies have since then been reported in the literature on Robin-like loose coupling for incompressible FSI involving thick-walled solids (see, e.g., [2, 18, 5, 21, 22]), but without rigorous error analysis nor convergence rates. In [17], it is shown that the generalized Robin-Neumann scheme of [18] introduces a splitting error scaling as $\mathcal{O}(\tau/h^{\frac{1}{2}})$, which requires a $\tau \lesssim h^{\frac{3}{2}}$ condition for accuracy (not for stability).

In [10], the Robin coefficient inherited the $\mathcal{O}(h^{-1})$ scaling from Nitsche's method, but it was noted numerically that this scaling appeared not to be necessary for the stability of the algorithm. In a recent development [8], it was shown for a semi-discretization in time that the coupling scheme indeed is stable independent of the added mass effect and an error estimate of order $\mathcal{O}(\tau^{\frac{1}{2}})$, where τ denotes the time step, was shown. Another result in this spirit was reported in [27], for a fully discrete Robin-Robin method and under a CFL-like condition on the discretization parameters. A stability estimate for the time semi-discretized problem with moving fluid domain is also provided, but the treatment of the convective term involves an artificial modification of the fluid velocity on the interface. An alternative fully discrete formulation is introduced in [6], where the stresses are represented in terms of Lagrange multipliers or variational residuals, and the exponential growth of the stability factor was moderated to sub-linear growth without conditions on the discretization parameters. Finally, both for the cases of parabolic-parabolic and parabolic-hyperbolic couplings, it was shown in [7] that in most situations one can expect the nearly-optimal order $\mathcal{O}\big(\tau\sqrt{1+\log\tau^{-1}}\big)$. Depending on the physical parameters however it was noted that this may not be attained, except for very small time steps unless the parameter in the Robin condition is chosen carefully.

The objective of the present paper is to build on the results of [6, 7] and extend them to more realistic settings, showing that the Robin-Robin loose coupling is indeed expected to result in a first order time discretization scheme also in physically relevant situations. The scientific contributions of this work are three fold. First, in a fully non-linear setting (coupling viscous incompressible flow in moving domains with the dynamics of an hyper-elastic solid), we provide a rigorous fully discrete formulation with suitable stabilization terms which guarantee unconditional energy stability. Second, in the linear case, we present the extension of the nearly-optimal error analysis from [7] to the case of the Stokes-elasticity system. To the best of our knowledge, this is the first time that such accuracy is proved for a loosely coupled scheme in incompressible fluid-structure interaction involving thick-walled solids. The latter results were first reported in [13, Chapter 5] and, therefore, the proofs are only sketched herein. Finally, the accuracy properties of the proposed method are illustrated in a series of well-known numerical examples. We in particular investigate the dependence of the accuracy on the physical parameters and the choice of the free parameter in the Robin coupling.

The rest of the paper is organized as follows. In Section 2, we introduce the considered physically realistic setting. We show how to extend the fully discrete formulation of [6] to this nonlinear case and prove the fundamental stability estimate in Section 3. Section 4 is devoted to the derivation of the nearly-optimal error estimate in a simplified linear setting. Finally, the paper is ended with some numerical examples which are reported in Section 5.

2. Problem setting. We consider a fluid-structure interaction system in which the fluid is modeled by the incompressible Navier-Stokes equations, in arbitrary Lagrangian-Eulerian (ALE) formalism, and the solid by the non-linear elastodynamics equations. The reference configuration of system is given by the domain $\Omega \overset{\text{def}}{=} \Omega^{\text{f}} \cup \Omega^{\text{s}} \subset \mathbb{R}^d$, with $d = 2, 3$. For all time $t > 0$, the current solid configuration is denoted by $\Omega^{\text{s}}(t) \subset \mathbb{R}^d$, whereas $\Omega^{\text{f}}(t) \subset \mathbb{R}^d$ stands for the moving fluid control volume. We denote by $\Sigma(t) \overset{\text{def}}{=} \partial\Omega^{\text{f}}(t) \cap \partial\Omega^{\text{s}}(t)$ the current configuration of the fluid-structure interface, whose reference configurations corresponds to $\Sigma \overset{\text{def}}{=} \partial\Omega^{\text{f}} \cap \partial\Omega^{\text{s}}$. The remaining parts of the fluid and solid boundaries are supposed to be time independent and partitioned as $\partial\Omega^{\text{f}} = \Gamma^{\text{f}} \cup \Sigma$ and $\partial\Omega^{\text{s}} = \Gamma^{\text{s}} \cup \Sigma$.

The moving fluid domain $\Omega^{\text{f}}(t)$ can be parametrized in terms of the so-called ALE map, $\boldsymbol{\mathcal{A}} : \Omega^{\text{f}} \times \mathbb{R}^+ \to \mathbb{R}^d$, in such a way that $\Omega^{\text{f}}(t) = \boldsymbol{\mathcal{A}}(\Omega^{\text{f}}, t)$. The ALE deformation map $\boldsymbol{\mathcal{A}}$ is often written in terms of fluid domain displacement $\boldsymbol{d}^{\text{f}} : \Omega^{\text{f}} \times \mathbb{R}^+ \to \mathbb{R}^d$ via the relation $\boldsymbol{\mathcal{A}} = \boldsymbol{I}_{\Omega^{\text{f}}} + \boldsymbol{d}^{\text{f}}$, where $\boldsymbol{I}_{\Omega^{\text{f}}}$ stands for the identity operator in Ω^{f}. We can hence introduce the notation $\boldsymbol{\mathcal{A}}_t \overset{\text{def}}{=} \boldsymbol{\mathcal{A}}(\cdot, t)$, the fluid domain velocity $\boldsymbol{w} \overset{\text{def}}{=} \partial_t \boldsymbol{\mathcal{A}} = \partial_t \boldsymbol{d}^{\text{f}}$, the fluid gradient of deformation $\boldsymbol{F} \overset{\text{def}}{=} \boldsymbol{\nabla}\boldsymbol{\mathcal{A}}$ (spatial gradient) and its Jacobian $J \overset{\text{def}}{=} \det \boldsymbol{F}$. For a given field f defined in the current configuration $\Omega^{\text{f}}(t)$, we shall use the notation $\widehat{f}$ to defined its corresponding ALE description in Ω^{f}, by composing with the ALE map, namely,

$$\widehat{f}(\boldsymbol{x}, t) \overset{\text{def}}{=} f(\boldsymbol{\mathcal{A}}(\boldsymbol{x}, t), t) \quad \forall \boldsymbol{x} \in \Omega^{\text{f}}.$$

Conversely, a given field defined in the reference configuration Ω^{f} can also be transported into the current configuration by composition with $\boldsymbol{\mathcal{A}}_t^{-1}$. For the sake of simplicity, this composition is omitted. For instance, $\boldsymbol{w}$ in $(2.1)_1$ below has to be read as $\boldsymbol{w} \circ \boldsymbol{\mathcal{A}}_t^{-1}$.

Coupled problem in strong form. The considered fluid-structure interaction model reads as follows: find the fluid domain displacement $\boldsymbol{d}^{\text{f}} : \Omega^{\text{f}} \times \mathbb{R}^+ \to \mathbb{R}^d$, the fluid velocity $\widehat{\boldsymbol{u}} : \Omega^{\text{f}} \times \mathbb{R}^+ \to \mathbb{R}^d$, the fluid pressure $\widehat{p} : \Omega^{\text{f}} \times \mathbb{R}^+ \to \mathbb{R}$, the solid displacement $\boldsymbol{d} : \Omega^{\text{s}} \times \mathbb{R}^+ \to \mathbb{R}^d$, and the structure velocity $\dot{\boldsymbol{d}} : \Omega^{\text{s}} \times \mathbb{R}^+ \to \mathbb{R}^d$ such that, for all $t > 0$,

$$\begin{cases} \rho^{\text{f}} \partial_t \boldsymbol{u}|_{\boldsymbol{\mathcal{A}}} + \rho^{\text{f}} (\boldsymbol{u} - \boldsymbol{w}) \cdot \boldsymbol{\nabla}\boldsymbol{u} - \mathbf{div}\, \boldsymbol{\sigma}(\boldsymbol{u}, p) = \boldsymbol{0} & \text{in} \quad \Omega^{\text{f}}(t), \\ \qquad\qquad\qquad\qquad\qquad\qquad \operatorname{div} \boldsymbol{u} = 0 & \text{in} \quad \Omega^{\text{f}}(t), \\ \qquad\qquad\qquad\qquad\qquad\qquad \boldsymbol{u} = \boldsymbol{0} & \text{on} \quad \Gamma^{\text{f}}, \end{cases} \tag{2.1}$$

$$\begin{cases} \rho^{\text{s}} \partial_t \dot{\boldsymbol{d}} - \mathbf{div}\left(\boldsymbol{F}^{\text{s}} \boldsymbol{\Sigma}(\boldsymbol{d})\right) = \boldsymbol{0} & \text{in} \quad \Omega^{\text{s}}, \\ \qquad\qquad\qquad\qquad\qquad\qquad \dot{\boldsymbol{d}} = \partial_t \boldsymbol{d} & \text{in} \quad \Omega^{\text{s}}, \\ \qquad\qquad\qquad\qquad\qquad\qquad \boldsymbol{d} = \boldsymbol{0} & \text{on} \quad \Gamma^{\text{s}}, \end{cases} \tag{2.2}$$

$$\begin{cases} \boldsymbol{d}^{\text{f}} = \boldsymbol{\mathcal{L}}\left(\boldsymbol{d}|_{\Sigma}\right), \quad \boldsymbol{w} = \partial_t \boldsymbol{d}^{\text{f}}, \quad \boldsymbol{\mathcal{A}} = \boldsymbol{I}_{\Omega^{\text{f}}} + \boldsymbol{d}^{\text{f}}, \quad \Omega^{\text{f}}(t) = \boldsymbol{\mathcal{A}}(\Omega^{\text{f}}, t), \\ \qquad\qquad\qquad\qquad\qquad\qquad \widehat{\boldsymbol{u}} = \dot{\boldsymbol{d}} \quad \text{on} \quad \Sigma, \\ \qquad\qquad\qquad\qquad\qquad\qquad \boldsymbol{F}^{\text{s}} \boldsymbol{\Sigma}(\boldsymbol{d}) \boldsymbol{n}^{\text{s}} = -J \widehat{\boldsymbol{\sigma}}(\boldsymbol{u}, p) \boldsymbol{F}^{-\text{T}} \widehat{\boldsymbol{n}} \quad \text{on} \quad \Sigma. \end{cases} \tag{2.3}$$

The constants $\rho^{\text{f}}, \rho^{\text{s}} > 0$ stand, respectively, for the fluid and solid densities, $\partial_t|_{\boldsymbol{\mathcal{A}}} \overset{\text{def}}{=} \partial_t + \boldsymbol{w} \cdot \boldsymbol{\nabla}$ for the ALE time derivative and $\boldsymbol{\sigma}(\boldsymbol{u}, p) \overset{\text{def}}{=} 2\mu\boldsymbol{\epsilon}(\boldsymbol{u}) - p\boldsymbol{I}$ for the fluid

Cauchy stress tensor, with $\mu > 0$ the fluid dynamic viscosity (supposed constant) and $\boldsymbol{\epsilon}(\boldsymbol{u}) = \frac{1}{2}(\boldsymbol{\nabla u} + (\boldsymbol{\nabla u})^{\mathrm{T}})$ the strain rate tensor. The symbol $\boldsymbol{F}^{\mathrm{s}} \stackrel{\mathrm{def}}{=} \boldsymbol{I} + \boldsymbol{\nabla d}$ corresponds to the gradient of deformation of the solid and $\boldsymbol{\Sigma}(\boldsymbol{d})$ denotes its second Piola-Kirchoff stress tensor which, for an hyper-elastic material, is given in terms of the internal energy functional $W : \mathbb{R}^{d\times d}_{\mathrm{sym}} \to \mathbb{R}^{+}$ as

$$\boldsymbol{\Sigma} = \frac{\partial W}{\partial \boldsymbol{E}}(\boldsymbol{E}),$$

where the symbol $\boldsymbol{E}$ denotes the Green-Lagrange strain tensor given by the relation $\boldsymbol{E} \stackrel{\mathrm{def}}{=} \frac{1}{2}\big((\boldsymbol{F}^{\mathrm{s}})^{\mathrm{T}}\boldsymbol{F}^{\mathrm{s}} - \boldsymbol{I}\big)$.

Finally, the coupled system (2.1)-(2.3) is complemented with the following initial conditions $\widehat{\boldsymbol{u}}(0) = \widehat{\boldsymbol{u}}_0$ and $\boldsymbol{d}(0) = \boldsymbol{d}_0, \dot{\boldsymbol{d}}(0) = \dot{\boldsymbol{d}}_0$ in Ω^{f} and Ω^{s}, respectively.

The relation $(2.3)_1$ enforces the geometrical compatibility between the fluid and solid domains. Here, the symbol $\boldsymbol{\mathcal{L}}$ represents a smooth lifting operator (possibly non-linear) from Σ over Ω^{f}, which vanishes on Γ^{f}. The remaining interface conditions $(2.3)_{2,3}$ enforce, respectively, the so-called interface kinematic and dynamic coupling.

Weak form and energy identity. We consider the following functional spaces:

$$\boldsymbol{V}^{\mathrm{f}} \subset \big\{\boldsymbol{v} \in \boldsymbol{H}^1(\Omega^{\mathrm{f}}) \,:\, \boldsymbol{v}|_{\Gamma^{\mathrm{f}}} = \boldsymbol{0}\big\}, \quad M^{\mathrm{f}} \stackrel{\mathrm{def}}{=} L^2(\Omega^{\mathrm{f}}), \quad \boldsymbol{V}^{\mathrm{s}} \subset \big\{\boldsymbol{v} \in \boldsymbol{H}^1(\Omega^{\mathrm{s}}) \,:\, \boldsymbol{v}|^{\mathrm{s}}_{\Gamma} = \boldsymbol{0}\big\}.$$

Let $\big(\widehat{\boldsymbol{u}}, \widehat{p}, \boldsymbol{d}, \dot{\boldsymbol{d}}\big)$ be solution of the coupled system (2.1)–(2.3), one can show that the following monolithic variational formulation holds (see, e.g., [16]), for $t > 0$,

(2.4)

$$\begin{aligned}
&\rho^{\mathrm{f}}\frac{\mathrm{d}}{\mathrm{d}t}\int_{\Omega^{\mathrm{f}}(t)} \boldsymbol{u}\cdot\boldsymbol{v} - \rho^{\mathrm{f}}\int_{\Omega^{\mathrm{f}}(t)} (\operatorname{div}\boldsymbol{w})\boldsymbol{u}\cdot\boldsymbol{v} + \rho^{\mathrm{f}}\int_{\Omega^{\mathrm{f}}(t)} (\boldsymbol{u}-\boldsymbol{w})\cdot\boldsymbol{\nabla u}\cdot\boldsymbol{v} + 2\mu\int_{\Omega^{\mathrm{f}}(t)} \boldsymbol{\epsilon}(\boldsymbol{u}) : \boldsymbol{\epsilon}(\boldsymbol{v}) \\
&\qquad - \int_{\Omega^{\mathrm{f}}(t)} p\operatorname{div}\boldsymbol{v} + \int_{\Omega^{\mathrm{f}}(t)} q\operatorname{div}\boldsymbol{u} + \rho^{\mathrm{s}}\int_{\Omega^{\mathrm{s}}} \partial_t\dot{\boldsymbol{d}}\cdot\boldsymbol{\xi} + \int_{\Omega^{\mathrm{s}}} \boldsymbol{\Sigma} : \partial_{\boldsymbol{d}}(\boldsymbol{E})\boldsymbol{\xi} = 0
\end{aligned}$$

for all $(\widehat{\boldsymbol{v}}, \widehat{q}, \boldsymbol{\xi}) \in \boldsymbol{V}^{\mathrm{f}} \times M^{\mathrm{f}} \times \boldsymbol{V}^{\mathrm{s}}$ with $\widehat{\boldsymbol{v}}|_{\Sigma} = \boldsymbol{\xi}|_{\Sigma}$, and where we have used the notation

$$\partial_{\boldsymbol{d}}(\boldsymbol{E})\boldsymbol{\xi} \stackrel{\mathrm{def}}{=} \frac{1}{2}\Big[\big(\boldsymbol{F}^{\mathrm{s}}\big)^{\mathrm{T}}\boldsymbol{\nabla\xi} + \big(\boldsymbol{\nabla\xi}\big)^{\mathrm{T}}\boldsymbol{F}^{\mathrm{s}}\Big], \tag{2.5}$$

for the differential of $\boldsymbol{E}$ applied to $\boldsymbol{\xi}$.

By testing (2.4) with $(\widehat{\boldsymbol{v}}, \widehat{q}, \boldsymbol{\xi}) = (\widehat{\boldsymbol{u}}, \widehat{p}, \dot{\boldsymbol{d}})$ and using standard arguments, we can obtain the following classical energy identity (see, e.g., [16]):

$$\begin{aligned}
&\frac{\rho^{\mathrm{f}}}{2}\|\boldsymbol{u}\|^2_{0,\Omega^{\mathrm{f}}(t)} + \frac{\rho^{\mathrm{s}}}{2}\|\dot{\boldsymbol{d}}\|^2_{0,\Omega^{\mathrm{s}}} + \int_{\Omega^{\mathrm{s}}} W\big(\boldsymbol{E}(\boldsymbol{d})\big) + 2\mu\int_0^t \|\boldsymbol{\epsilon}(\boldsymbol{u}(s))\|^2_{0,\Omega^{\mathrm{f}}(s)}\mathrm{d}s \\
&\qquad = \frac{\rho^{\mathrm{f}}}{2}\|\boldsymbol{u}_0\|^2_{0,\Omega^{\mathrm{f}}(0)} + \frac{\rho^{\mathrm{s}}}{2}\|\dot{\boldsymbol{d}}_0\|^2_{0,\Omega^{\mathrm{s}}} + \frac{1}{2}\int_{\Omega^{\mathrm{s}}} W\big(\boldsymbol{E}(\boldsymbol{d}_0)\big).
\end{aligned} \tag{2.6}$$

Here, the first two terms represent the kinetic energy of the fluid and solid, respectively. The third term takes into account the hyperelastic energy of the solid, and the fourth term corresponds to the viscous dissipation of the fluid.

3. Robin-Robin explicit coupling scheme. The purpose of this section is to formulate the Robin-Robin loosely coupled scheme of [6, 8] in the framework of the non-linear coupled problem (2.1)-(2.3).

Time semi-discretization. In what follows, the scalar $\tau > 0$ denotes the time-step length and $\{t_n \overset{\text{def}}{=} n\tau\}_{n\in\mathbb{N}}$ represents the temporal grid. We shall also make use of the following notations:

$$\partial_\tau x^n \overset{\text{def}}{=} \frac{1}{\tau}(x^n - x^{n-1}), \quad x^{n-\frac{1}{2}} \overset{\text{def}}{=} \frac{1}{2}(x^n + x^{n-1}),$$

for the first-order backward difference and the mid-point value, respectively. Moreover, for a given time-dependent quantity $x(t)$, we will use the notation $x^n \overset{\text{def}}{=} x(t_n)$.

The bulk terms of the fluid sub-system (2.1) will be discretized in time with a backward-Euler semi-implicit scheme, whereas for the solid sub-system (2.2) we consider a mid-point scheme with the so-called Gonzalez correction (see [23]). Finally, for the time discretization of the interface conditions (2.3), we combine an explicit treatment of the geometrical compatibility with a Robin-Robin type splitting of the kinematic and dynamic interface conditions, originally proposed in [8] for the linear case. By introducing the following notation for the interfacial fluid stresses on the reference configuration,

$$\boldsymbol{\lambda}^n \overset{\text{def}}{=} J^n \widehat{\boldsymbol{\sigma}}(\boldsymbol{u}^n, p^n)\big(\boldsymbol{F}^n\big)^{-\mathrm{T}} \widehat{\boldsymbol{n}} \quad \text{on} \quad \Sigma, \tag{3.1}$$

the resulting time-stepping procedure can formally be written as follows:

- Solve solid:

$$\begin{cases} \rho^{\mathrm{s}} \partial_\tau \dot{\boldsymbol{d}}^n - \mathbf{div}\left(\boldsymbol{F}^{\mathrm{s},n-\frac{1}{2}} \bar{\boldsymbol{\Sigma}}^{n-\frac{1}{2}}\right) = \boldsymbol{0} & \text{in} \quad \Omega^{\mathrm{s}}, \\ \dot{\boldsymbol{d}}^{n-\frac{1}{2}} = \partial_\tau \boldsymbol{d}^n & \text{in} \quad \Omega^{\mathrm{s}}, \\ \boldsymbol{d}^n = \boldsymbol{0} & \text{on} \quad \Gamma^{\mathrm{s}}, \\ \boldsymbol{F}^{\mathrm{s,n}-\frac{1}{2}} \bar{\boldsymbol{\Sigma}}^{n-\frac{1}{2}} \boldsymbol{n}^{\mathrm{s}} + \alpha\big(\dot{\boldsymbol{d}}^{n-\frac{1}{2}} - \widehat{\boldsymbol{u}}^{n-1}\big) = -\boldsymbol{\lambda}^{n-1} & \text{on} \quad \Sigma. \end{cases} \tag{3.2}$$

- Fluid domain update:

$$\boldsymbol{d}^{\mathrm{f},n} = \boldsymbol{\mathcal{L}}\left(\boldsymbol{d}^n|_\Sigma\right), \quad \boldsymbol{w}^n = \partial_\tau \boldsymbol{d}^{\mathrm{f},n}, \quad \boldsymbol{\mathcal{A}}^n = \boldsymbol{I}_{\Omega^{\mathrm{f}}} + \boldsymbol{d}^{\mathrm{f},n}, \quad \Omega^{\mathrm{f},n} = \boldsymbol{\mathcal{A}}^n(\Omega^{\mathrm{f}}). \tag{3.3}$$

- Solve fluid:

$$\begin{cases} \rho^{\mathrm{f}} \partial_\tau \boldsymbol{u}^n|_{\boldsymbol{\mathcal{A}}} + \rho^{\mathrm{f}}(\boldsymbol{u}^{n-1} - \boldsymbol{w}^n) \cdot \boldsymbol{\nabla} \boldsymbol{u}^n - \mathbf{div}\, \boldsymbol{\sigma}(\boldsymbol{u}^n, p^n) = \boldsymbol{0} & \text{in} \quad \Omega^{\mathrm{f},n}, \\ \operatorname{div} \boldsymbol{u}^n = 0 & \text{in} \quad \Omega^{\mathrm{f},n}, \\ \boldsymbol{u}^n = \boldsymbol{0} & \text{on} \quad \Gamma^{\mathrm{f}}, \\ \boldsymbol{\lambda}^n + \alpha\big(\widehat{\boldsymbol{u}}^n - \dot{\boldsymbol{d}}^{n-\frac{1}{2}}\big) = \boldsymbol{\lambda}^{n-1} & \text{on} \quad \Sigma. \end{cases} \tag{3.4}$$

Here, the symbol $\bar{\boldsymbol{\Sigma}}^{n-\frac{1}{2}}$ denotes the mid-point correction of the solid stress given by (see [23]):

$$\bar{\boldsymbol{\Sigma}}^{n-\frac{1}{2}} \overset{\text{def}}{=} \boldsymbol{\Sigma}^{n-\frac{1}{2}} + \frac{\partial_\tau W(\boldsymbol{E}^n) - \dfrac{\partial W}{\partial \boldsymbol{E}}\big(\boldsymbol{E}^{n-\frac{1}{2}}\big) : \partial_\tau \boldsymbol{E}^n}{|\partial_\tau \boldsymbol{E}^n|^2} \partial_\tau \boldsymbol{E}^n, \tag{3.5}$$

which guarantees energy stability in the solid, and the scalar $\alpha > 0$ stands for the user-defined Robin parameter of the fluid-solid splitting. Note that the above interfacial

Robin-Robin splitting, viz.,

$$\begin{cases} \boldsymbol{F}^{\mathrm{s,n-\frac{1}{2}}}\bar{\boldsymbol{\Sigma}}^{n-\frac{1}{2}}\boldsymbol{n}^{\mathrm{s}} + \alpha\big(\dot{\boldsymbol{d}}^{n-\frac{1}{2}} - \widehat{\boldsymbol{u}}^{n-1}\big) = -\boldsymbol{\lambda}^{n-1} & \text{on} \quad \Sigma, \\ \boldsymbol{\lambda}^{n} + \alpha\big(\widehat{\boldsymbol{u}}^{n} - \dot{\boldsymbol{d}}^{n-\frac{1}{2}}\big) = \boldsymbol{\lambda}^{n-1} & \text{on} \quad \Sigma, \end{cases} \tag{3.6}$$

is written in the reference configuration of the interface.

Space discretization, fully discrete scheme. For the spatial discretization of (3.2)–(3.4), we adopt a finite element approximation. Let $\mathcal{T}_h^{\mathrm{f}}$ and $\mathcal{T}_h^{\mathrm{s}}$ be, respectively, simplicial triangulations of Ω^{f} and Ω^{s}. We assume that $\mathcal{T}_h^{\mathrm{f}}$ and $\mathcal{T}_h^{\mathrm{s}}$ match on the interface Σ. We then define the following finite element spaces:

$$\boldsymbol{V}_h^{\mathrm{s}} \stackrel{\mathrm{def}}{=} \big\{\boldsymbol{v} \in \boldsymbol{V}^{\mathrm{s}} : \boldsymbol{v}|_K \in \mathbb{P}^1(K), \forall K \in \mathcal{T}_h^{\mathrm{s}}\big\}, \quad \boldsymbol{V}_h^{\mathrm{f}} \stackrel{\mathrm{def}}{=} \big\{\boldsymbol{v} \in \boldsymbol{V}^{\mathrm{f}} : \boldsymbol{v}|_K \in \mathbb{P}^1(K), \forall K \in \mathcal{T}_h^{\mathrm{f}}\big\},$$

$$M_h^{\mathrm{f}} \stackrel{\mathrm{def}}{=} \big\{v \in M^{\mathrm{f}} : v|_K \in \mathbb{P}^1(K), \forall K \in \mathcal{T}_h^{\mathrm{f}}\big\},$$

Since the fluid and solid meshes are assumed to match at the interface, we can define the discrete traces space

$$\boldsymbol{V}_h^{\mathrm{g}} \stackrel{\mathrm{def}}{=} \mathrm{Tr}_\Sigma \boldsymbol{V}_h^{\mathrm{f}} = \mathrm{Tr}_\Sigma \boldsymbol{V}_h^{\mathrm{s}}. \tag{3.7}$$

The fluid bi-linear form is given by

$$\begin{aligned} a_{\Omega^{\mathrm{f},n}}\big(\boldsymbol{u}_h^{n-1}, \boldsymbol{w}_h^n; (\boldsymbol{u}_h^n, p_h^n), (\boldsymbol{v}_h, q_h)\big) \stackrel{\mathrm{def}}{=} & \rho^{\mathrm{f}} \int_{\Omega^{\mathrm{f},n}} (\boldsymbol{u}_h^{n-1} - \boldsymbol{w}_h^n) \cdot \boldsymbol{\nabla} \boldsymbol{u}_h^n \cdot \boldsymbol{v}_h \\ & + \frac{\rho^{\mathrm{f}}}{2} \int_{\Omega^{\mathrm{f},n}} (\operatorname{div} \boldsymbol{u}_h^{n-1}) \boldsymbol{u}_h^n \cdot \boldsymbol{v}_h \\ & - \frac{\rho^{\mathrm{f}}}{2} \int_{\Sigma^n} (\boldsymbol{u}_h^{n-1} - \dot{\boldsymbol{d}}_h^{n-\frac{1}{2}}) \cdot \boldsymbol{n} \boldsymbol{u}_h^n \cdot \boldsymbol{v}_h \\ & + 2\mu \int_{\Omega^{\mathrm{f},n}} \boldsymbol{\epsilon}_h(\boldsymbol{u}_h^n) : \boldsymbol{\epsilon}_h(\boldsymbol{v}_h) - \int_{\Omega^{\mathrm{f},n}} p_h^n \operatorname{div} \boldsymbol{v}_h \\ & + \int_{\Omega^{\mathrm{f},n}} q_h \operatorname{div} \boldsymbol{u}_h^n \\ & + s_h^{\mathrm{f}}\big(\boldsymbol{u}_h^{n-1}, \boldsymbol{w}_h^n; (\boldsymbol{u}_h^n, p_h^n), (\boldsymbol{v}_h, q_h)\big). \end{aligned} \tag{3.8}$$

The second term in (3.8) corresponds to the so-called Temam's trick, which copes with the fact that the discrete fluid velocities are not divergence free. The third term is a weakly consistent stabilization term which allows to control the energy contribuitons of the convective term (first term of (3.8)) induced by the fact that

$$\widehat{\boldsymbol{u}}_h^{n-1}|_\Sigma \neq \boldsymbol{w}_h^n|_\Sigma = \dot{\boldsymbol{d}}_h^{n-\frac{1}{2}}|_\Sigma.$$

Following [28, Chapter 5], we introduce a second weakly consistent stabilization term, namely,

$$s_{\Omega^{\mathrm{f},n}}(\boldsymbol{u}_h^n, \boldsymbol{v}_h) \stackrel{\mathrm{def}}{=} -\frac{\rho^{\mathrm{f}}}{2\tau}\left(\int_{\Omega^{\mathrm{f},n}} \boldsymbol{u}_h^n \cdot \boldsymbol{v}_h - \int_{\Omega^{\mathrm{f},n-1}} \boldsymbol{u}_h^n \cdot \boldsymbol{v}_h\right) + \frac{\rho^{\mathrm{f}}}{2} \int_{\Omega^{\mathrm{f},n}} (\operatorname{div} \boldsymbol{w}_h^n) \boldsymbol{u}_h^n \cdot \boldsymbol{v}_h, \tag{3.9}$$

whose purpose is to cope with the issues related to the so-called discrete geometric conservation law (see, e.g., [14]). Note that the weak consistency of (3.9) is a

consequence of the Reynolds transport formula:

$$\frac{\mathrm{d}}{\mathrm{d}t}\int_{\Omega^{\mathrm{f}}(t)} q = \int_{\Omega^{\mathrm{f}}(t)} q \,\mathrm{div}\, \boldsymbol{w}$$

for any smooth enough field $\widehat{q} : \Omega^{\mathrm{f}} \to \mathbb{R}^+$. Finally, the non-negative bi-linear term,

$$s_h^{\mathrm{f}}\big(\boldsymbol{u}_h^{n-1}, \boldsymbol{w}_h^n; (\boldsymbol{u}_h^n, p_h^n), (\boldsymbol{v}_h, q_h)\big),$$

stands for any given velocity and pressure stabilization operator (see, e.g., [29, 11]), whose purpose is to circumvent the issues related to the lack of robustness for both high local Reynolds numbers and the lack of inf-sup stability for the pair $\boldsymbol{V}_h^{\mathrm{f}}/M^{\mathrm{f}}$.

Algorithm 3.1 Explicit Robin-Robin scheme (fully discrete)

Assume $\boldsymbol{u}_h^0$, $\boldsymbol{d}_h^0$ and $\boldsymbol{d}_h^{\mathrm{f},0}$, $\boldsymbol{\lambda}_h^0$ to be given and, for $n \geqslant 1$, perform:

- Solve solid: find $(\boldsymbol{d}_h^n, \dot{\boldsymbol{d}}_h^n) \in \boldsymbol{V}_h^{\mathrm{s}} \times \boldsymbol{V}_h^{\mathrm{s}}$, with $\dot{\boldsymbol{d}}_h^{n-\frac{1}{2}} = \partial_\tau \boldsymbol{d}_h^n$ such that

$$\rho^{\mathrm{s}} \int_{\Omega^{\mathrm{s}}} \partial_\tau \dot{\boldsymbol{d}}_h^n \cdot \boldsymbol{\xi}_h + \int_{\Omega^{\mathrm{s}}} \bar{\boldsymbol{\Sigma}}_h^{n-\frac{1}{2}} : \partial_{\boldsymbol{d}}(\boldsymbol{E}_h^{n-\frac{1}{2}})\boldsymbol{\xi}_h + \alpha \int_\Sigma (\dot{\boldsymbol{d}}_h^{n-\frac{1}{2}} - \widehat{\boldsymbol{u}}_h^{n-1}) \cdot \boldsymbol{\xi}_h = -\int_\Sigma \boldsymbol{\lambda}_h^{n-1} \cdot \boldsymbol{\xi}_h \tag{3.10}$$

  for all $\boldsymbol{\xi}_h \in \boldsymbol{V}_h^{\mathrm{s}}$.
- Update fluid domain:

$$\boldsymbol{d}_h^{\mathrm{f},n} = \boldsymbol{\mathcal{L}}_h(\boldsymbol{d}_h^n|_\Sigma), \quad \boldsymbol{w}_h^n = \partial_\tau \boldsymbol{d}_h^{\mathrm{f},n}, \qquad \boldsymbol{\mathcal{A}}_h^n = \boldsymbol{I}_{\Omega^{\mathrm{f}}} + \boldsymbol{d}_h^{\mathrm{f},n}, \quad \Omega^{\mathrm{f},n} = \boldsymbol{\mathcal{A}}_h^n(\Omega^{\mathrm{f}}).$$

- Solve fluid: find $(\widehat{\boldsymbol{u}}^n, \widehat{p}^n) \in \boldsymbol{V}_h^{\mathrm{f}} \times Q_h$ such that

$$\begin{aligned}\frac{\rho^{\mathrm{f}}}{\tau}\left(\int_{\Omega^{\mathrm{f},n}} \boldsymbol{u}_h^n \cdot \boldsymbol{v}_h - \int_{\Omega^{\mathrm{f},n-1}} \boldsymbol{u}_h^{n-1} \cdot \boldsymbol{v}_h\right) - \rho^{\mathrm{f}} \int_{\Omega^{\mathrm{f},n}} (\mathrm{div}\, \boldsymbol{w}_h^n)\boldsymbol{u}_h^n \cdot \boldsymbol{v}_h \\ + s_{\Omega^{\mathrm{f},n}}(\boldsymbol{u}_h^n, \boldsymbol{v}_h) + a_{\Omega^{\mathrm{f},n}}\big(\boldsymbol{u}_h^{n-1}, \boldsymbol{w}_h^n; (\boldsymbol{u}_h^n, p_h^n), (\boldsymbol{v}_h, q_h)\big) \\ + \alpha \int_\Sigma (\widehat{\boldsymbol{u}}_h^n - \dot{\boldsymbol{d}}_h^{n-\frac{1}{2}}) \cdot \widehat{\boldsymbol{v}}_h = \int_\Sigma \boldsymbol{\lambda}_h^{n-1} \cdot \widehat{\boldsymbol{v}}_h\end{aligned} \tag{3.11}$$

  for all $(\widehat{\boldsymbol{v}}_h, \widehat{q}_h) \in \boldsymbol{V}_h^{\mathrm{f}} \times Q_h$.
- Fluid-stress update: set $\boldsymbol{\lambda}_h^n \in \boldsymbol{V}_h^{\mathrm{g}}$ as

$$\boldsymbol{\lambda}_h^n = \boldsymbol{\lambda}_h^{n-1} + \alpha\big(\dot{\boldsymbol{d}}_h^{n-\frac{1}{2}} - \widehat{\boldsymbol{u}}_h^n\big) \quad \text{on} \quad \Sigma. \tag{3.12}$$

With all the above ingredients, the proposed fully discrete counterpart of (3.2)–(3.4) is detailed in Algorithm 3.1.

Some remarks are now in order. The relation (3.12) in Algorithm 3.1 is essentially a rewriting of $(3.6)_2$, in which the intermediate variable $\boldsymbol{\lambda}_h^n$ represents the discrete counterpart of the interfacial fluid stress on the reference configuration $\boldsymbol{\lambda}^n$, given by (3.1). Indeed, by combining (3.11) and (3.12), the update of the fluid-stress in the fourth step of Algorithm 3.1 can be formulated, in a more standard form as a fluid

variational residual (see, e.g., [15]):

$$\int_\Sigma \boldsymbol{\lambda}_h^n \cdot \boldsymbol{\mu}_h = \frac{\rho^{\mathrm{f}}}{\tau}\left(\int_{\Omega^{\mathrm{f},n}} \boldsymbol{u}_h^n \cdot \boldsymbol{\mathcal{L}}_h^{\mathrm{f}}\boldsymbol{\mu}_h - \int_{\Omega^{\mathrm{f},n-1}} \boldsymbol{u}_h^{n-1} \cdot \boldsymbol{\mathcal{L}}_h^{\mathrm{f}}\boldsymbol{\mu}_h\right) \tag{3.13}$$

$$- \rho^{\mathrm{f}} \int_{\Omega^{\mathrm{f},n}} (\operatorname{div} \boldsymbol{w}_h^n)\boldsymbol{u}_h^n \cdot \boldsymbol{\mathcal{L}}_h^{\mathrm{f}}\boldsymbol{\mu}_h + a_{\Omega^{\mathrm{f},n}}\big(\boldsymbol{u}_h^{n-1}, \boldsymbol{w}_h^n; (\boldsymbol{u}_h^n, p_h^n), (\boldsymbol{\mathcal{L}}_h^{\mathrm{f}}\boldsymbol{\mu}_h, 0)\big)$$

for all $\boldsymbol{\mu}_h \in \boldsymbol{V}_h^{\mathrm{g}}$ and where $\boldsymbol{\mathcal{L}}_h^{\mathrm{f}} : \boldsymbol{V}_h^{\mathrm{g}} \to \boldsymbol{V}_h^{\mathrm{f}}$ represents a linear fluid-sided lifting operator, such that, the nodal values of $\mathcal{L}_h^{\mathrm{f}}\boldsymbol{\mu}_h$ vanish out of Σ and $(\boldsymbol{\mathcal{L}}_h^{\mathrm{f}}\boldsymbol{\mu}_h)|_\Sigma = \boldsymbol{\mu}_h$, for all $\boldsymbol{\mu}_h \in \boldsymbol{V}_h^{\mathrm{g}}$. We can hence see that, as indicated above, $\boldsymbol{\lambda}_h^n$ is nothing but the discrete counterpart of the interfacial fluid stress on the reference configuration. It is worth noting that the interfacial stabilization term in (3.8) introduces a weakly consistent perturbation of the fluid stresses approximation provided by (3.13). Indeed, this relation formally writes

$$\int_\Sigma \boldsymbol{\lambda}_h^n \cdot \boldsymbol{\mu}_h \equiv \int_{\Sigma^n} \boldsymbol{\sigma}(\boldsymbol{u}_h^n, p_h^n)\boldsymbol{n}_h \cdot \boldsymbol{\mu}_h - \frac{\rho^{\mathrm{f}}}{2}\int_{\Sigma^n} \big(\boldsymbol{u}_h^{n-1} - \dot{\boldsymbol{d}}_h^{n-\frac{1}{2}} \circ (\boldsymbol{\mathcal{A}}_h^n)^{-1}\big) \cdot \boldsymbol{n}_h(\boldsymbol{u}_h^n \cdot \boldsymbol{\mu}_h)$$

for all $\boldsymbol{\mu} \in \boldsymbol{V}_h^{\mathrm{g}}$, or point-wise

$$\boldsymbol{\lambda}^n \equiv J^n \widehat{\boldsymbol{\sigma}}(\boldsymbol{u}^n, p^n)(\boldsymbol{F}^n)^{-\mathrm{T}}\widehat{\boldsymbol{n}} - \frac{\rho^{\mathrm{f}} J^n}{2}(\widehat{\boldsymbol{u}}^{n-1} - \dot{\boldsymbol{d}}^{n-\frac{1}{2}}) \cdot \big((\boldsymbol{F}^n)^{-\mathrm{T}}\widehat{\boldsymbol{n}}\big)\widehat{\boldsymbol{u}}^n \quad \text{on} \quad \Sigma.$$

It should also be noted that these last two expressions are merely formal and, therefore, can not be used in the energy stability analysis of Algorithm 3.1, presented in Section 3.1 below.

Algorithm 3.1 shares some similarities with the time-semidiscrete Robin-Robin scheme proposed in [27], but with several fundamental differences. First, the method is here formulated in a fully discrete setting, with a rigorous definition of the interfacial fluid-stresses. Second, a suitable interfacial stabilization is added to control the energy contributions of the convective term. This avoids the artificial modifications of the fluid velocity on the interface advocated in [27, Section 3]. Third, the stability of the method reported in the next paragraph also holds in 3D, irrespectively of the discrete geometric conservation law, via the stabilization term (3.9). Finally, the stability analysis (Section 3.1) and the numerical examples (of Section 5) cover the case of the coupling with a general non-linear solid model.

3.1. Energy stability analysis. For $n \geqslant 1$, let the discrete energy and dissipation be respectively defined as

$$E_h^n \stackrel{\mathrm{def}}{=} \frac{\rho^{\mathrm{f}}}{2}\|\boldsymbol{u}_h^n\|_{0,\Omega^{\mathrm{f},n}}^2 + \frac{\rho^{\mathrm{s}}}{2}\|\dot{\boldsymbol{d}}_h^n\|_{0,\Omega^{\mathrm{s}}}^2 + \int_{\Omega^{\mathrm{s}}} W(\boldsymbol{E}_h^n) + \frac{\tau}{2}\left(\alpha\|\widehat{\boldsymbol{u}}_h^n\|_{0,\Sigma}^2 + \frac{1}{\alpha}\|\boldsymbol{\lambda}_h\|_{0,\Sigma}^2\right),$$

$$G_h^n \stackrel{\mathrm{def}}{=} \sum_{m=1}^{n} \tau\left(2\mu\|\boldsymbol{\epsilon}(\boldsymbol{u}_h^m)\|_{0,\Omega^{\mathrm{f},m}}^2 + \alpha\|\dot{\boldsymbol{d}}_h^{m-\frac{1}{2}} - \widehat{\boldsymbol{u}}_h^{m-1}\|_{0,\Sigma}^2\right).$$

THEOREM 1. *Let $\big\{(\widehat{\boldsymbol{u}}^n, \widehat{p}^n, \boldsymbol{d}^n, \dot{\boldsymbol{d}}^n, \boldsymbol{\lambda}^n\big\}_{n\geqslant 1}$ be given by Algorithm 3.1. The following energy estimate holds for $n \geqslant 1$*

$$E_h^n + G_h^n \leqslant E_h^0. \tag{3.14}$$

As a result, Algorithm 3.1 is unconditionally stable in the energy norm.

Proof. We proceed by testing (3.10) with $\boldsymbol{\xi}_h = \dot{\boldsymbol{d}}_h^{n-\frac{1}{2}}$ and (3.11) with $(\widehat{\boldsymbol{v}}_h, \widehat{q}_h) = (\widehat{\boldsymbol{u}}_h^n, \widehat{p}_h^n)$. For the solid, we get

$$\frac{\rho^{\mathrm{s}}}{2}\partial_\tau \|\dot{\boldsymbol{d}}_h^n\|^2_{0,\Omega^{\mathrm{s}}} + \int_{\Omega^{\mathrm{s}}} \bar{\boldsymbol{\Sigma}}_h^{n-\frac{1}{2}} : \partial_{\boldsymbol{d}}(\boldsymbol{E}_h^{n-\frac{1}{2}})\dot{\boldsymbol{d}}_h^{n-\frac{1}{2}} + \alpha \int_\Sigma (\dot{\boldsymbol{d}}_h^{n-\frac{1}{2}} - \widehat{\boldsymbol{u}}_h^{n-1}) \cdot \dot{\boldsymbol{d}}_h^{n-\frac{1}{2}} = -\int_\Sigma \boldsymbol{\lambda}_h^{n-1} \cdot \dot{\boldsymbol{d}}_h^{n-\frac{1}{2}}. \tag{3.15}$$

From (2.5), we have

$$\begin{aligned}
\partial_{\boldsymbol{d}}(\boldsymbol{E}_h^{n-\frac{1}{2}})\dot{\boldsymbol{d}}_h^{n-\frac{1}{2}} =& \frac{1}{2}\left((\boldsymbol{F}_h^{\mathrm{s},n-\frac{1}{2}})^{\mathrm{T}}\partial_\tau \boldsymbol{F}_h^{\mathrm{s},n} + (\partial_\tau \boldsymbol{F}_h^{\mathrm{s},n})^{\mathrm{T}}\boldsymbol{F}_h^{\mathrm{s},n-\frac{1}{2}}\right) \\
=& \frac{1}{2\tau}\left((\boldsymbol{F}_h^{\mathrm{s},n})^{\mathrm{T}}\boldsymbol{F}_h^{\mathrm{s},n} - (\boldsymbol{F}_h^{\mathrm{s},n-1})^{\mathrm{T}}\boldsymbol{F}_h^{\mathrm{s},n-1}\right) \\
=& \partial_\tau \boldsymbol{E}_h^n.
\end{aligned}$$

So that, by inserting the previous relation into (3.15) and using the definition of the stress correction (3.5), we have

$$\int_{\Omega^{\mathrm{s}}} \bar{\boldsymbol{\Sigma}}_h^{n-\frac{1}{2}} : \partial_\tau \boldsymbol{E}_h^n = \int_{\Omega^{\mathrm{s}}} \partial_\tau W(\boldsymbol{E}_h^n). \tag{3.16}$$

By inserting (3.16) into (3.15), we ultimately arrive at:

$$\frac{\rho^{\mathrm{s}}}{2}\partial_\tau \|\dot{\boldsymbol{d}}_h^n\|^2_{0,\Omega^{\mathrm{s}}} + \partial_\tau \int_{\Omega^{\mathrm{s}}} W(\boldsymbol{E}_h^n) + \alpha \int_\Sigma (\dot{\boldsymbol{d}}_h^{n-\frac{1}{2}} - \widehat{\boldsymbol{u}}_h^{n-1}) \cdot \dot{\boldsymbol{d}}_h^{n-\frac{1}{2}} = -\int_\Sigma \boldsymbol{\lambda}_h^{n-1} \cdot \dot{\boldsymbol{d}}_h^{n-\frac{1}{2}}. \tag{3.17}$$

For the fluid, the bulk terms are treated in a standard fashion (see [16, Proposition 9.4] and [28, Chapter 5]) with the sole differences in the control of the ALE time derivative and of the convective terms, with the considered stabilizations. Using integration by parts, the fact that (by construction) $\boldsymbol{w}_h^n|_\Sigma = \dot{\boldsymbol{d}}_h^{n-\frac{1}{2}}|_\Sigma$ and the positiveness of s_h^{f}, we have

$$\begin{aligned}
a_{\Omega^{\mathrm{f},n}}\left(\boldsymbol{u}_h^{n-1}, \boldsymbol{w}_h^n; (\boldsymbol{u}_h^n, p_h^n), (\boldsymbol{u}_h^n, p_h^n)\right) \geqslant\ & 2\mu \|\boldsymbol{\epsilon}(\boldsymbol{u}_h^n)\|^2_{0,\Omega^{\mathrm{f},n}} \\
&+ \frac{\rho^{\mathrm{f}}}{2}\int_{\Omega^{\mathrm{f},n}} (\boldsymbol{u}_h^{n-1} - \boldsymbol{w}_h^n)\cdot \boldsymbol{\nabla}|\boldsymbol{u}_h^n|^2 + \frac{\rho^{\mathrm{f}}}{2}\int_{\Omega^{\mathrm{f},n}} (\operatorname{div} \boldsymbol{u}_h^{n-1})|\boldsymbol{u}_h^n|^2 \\
&- \frac{\rho^{\mathrm{f}}}{2}\int_{\Sigma^n} (\boldsymbol{u}_h^{n-1} - \dot{\boldsymbol{d}}_h^{n-\frac{1}{2}})\cdot \boldsymbol{n}|\boldsymbol{u}_h^n|^2 \\
=\ & 2\mu \|\boldsymbol{\epsilon}(\boldsymbol{u}_h^n)\|^2_{0,\Omega^{\mathrm{f},n}} + \frac{\rho^{\mathrm{f}}}{2}\int_{\Omega^{\mathrm{f},n}} (\operatorname{div} \boldsymbol{w}_h^n)|\boldsymbol{u}_h^n|^2.
\end{aligned} \tag{3.18}$$

Using (3.12) and the arguments reported in [16, Proposition 9.4] and [28, Chapter 5], we finally obtain

$$\frac{\rho^{\mathrm{f}}}{2}\partial_\tau \|\boldsymbol{u}_h^n\|^2_{0,\Omega^{\mathrm{f},n}} + 2\mu \|\boldsymbol{\epsilon}(\boldsymbol{u}_h^n)\|^2_{0,\Omega^{\mathrm{f},n}} \leqslant \int_\Sigma \boldsymbol{\lambda}_h^{n-1}\cdot \widehat{\boldsymbol{u}}_h^n - \alpha \int_\Sigma (\widehat{\boldsymbol{u}}_h^n - \dot{\boldsymbol{d}}_h^{n-\frac{1}{2}})\cdot \widehat{\boldsymbol{u}}_h^n = \int_\Sigma \boldsymbol{\lambda}_h^n \cdot \widehat{\boldsymbol{u}}_h^n. \tag{3.19}$$

Next, we proceed to add the energy contributions of the solid, as given by (3.17), and the fluid, as expressed in (3.19). This results in the following energy expression:

$$\frac{\rho^{\mathrm{f}}}{2}\partial_\tau\|\boldsymbol{u}_h^n\|^2_{0,\Omega^{\mathrm{f},n}} + \frac{\rho^{\mathrm{s}}}{2}\partial_\tau\|\dot{\boldsymbol{d}}_h^n\|^2_{0,\Omega^{\mathrm{s}}} + \partial_\tau\int_{\Omega^{\mathrm{s}}} W(\boldsymbol{E}_h^n) + 2\mu\|\boldsymbol{\epsilon}(\boldsymbol{u}_h^n)\|^2_{0,\Omega^{\mathrm{f},n}} \leqslant R_h^n, \tag{3.20}$$

where

$$R_h^n \stackrel{\mathrm{def}}{=} \alpha\int_\Sigma(\widehat{\boldsymbol{u}}_h^{n-1} - \dot{\boldsymbol{d}}_h^{n-\frac{1}{2}})\cdot\dot{\boldsymbol{d}}_h^{n-\frac{1}{2}} - \int_\Sigma \boldsymbol{\lambda}_h^{n-1}\cdot\dot{\boldsymbol{d}}_h^{n-\frac{1}{2}} + \int_\Sigma \boldsymbol{\lambda}_h^n\cdot\widehat{\boldsymbol{u}}_h^n.$$

We can now proceed as in the case with a fixed domain [6], which yields

$$R_h^n = \frac{\alpha}{2}(\|\widehat{\boldsymbol{u}}_h^{n-1}\|^2_{0,\Sigma} - \|\widehat{\boldsymbol{u}}_h^n\|^2_{0,\Sigma}) + \frac{1}{2\alpha}(\|\boldsymbol{\lambda}_h^{n-1}\|^2_{0,\Sigma} - \|\boldsymbol{\lambda}_h^n\|^2_{0,\Sigma}) - \alpha\|\dot{\boldsymbol{d}}_h^{n-\frac{1}{2}} - \widehat{\boldsymbol{u}}_h^{n-1}\|^2_{0,\Sigma}, \tag{3.21}$$

Finally, by inserting (3.21) into (3.20), we obtain

$$\begin{aligned}&\frac{\rho^{\mathrm{f}}}{2}\partial_\tau\|\boldsymbol{u}_h^n\|^2_{0,\Omega^{\mathrm{f},n}} + \frac{\rho^{\mathrm{s}}}{2}\partial_\tau\|\dot{\boldsymbol{d}}_h^n\|^2_{0,\Omega^{\mathrm{s}}} + \partial_\tau\int_{\Omega^{\mathrm{s}}} W(\boldsymbol{E}_h^n) + 2\mu\|\boldsymbol{\epsilon}(\boldsymbol{u}_h^n)\|^2_{0,\Omega^{\mathrm{f},n}}\\ &+ \frac{\alpha}{2}\|\widehat{\boldsymbol{u}}_h^n\|^2_{0,\Sigma} + \frac{\tau}{2\alpha}\|\boldsymbol{\lambda}_h^n\|^2_{0,\Sigma} + \alpha\|\dot{\boldsymbol{d}}_h^{n-\frac{1}{2}} - \widehat{\boldsymbol{u}}_h^{n-1}\|^2_{0,\Sigma} \leqslant \frac{\alpha}{2}\|\widehat{\boldsymbol{u}}_h^{n-1}\|^2_{0,\Sigma} + \frac{1}{2\alpha}\|\boldsymbol{\lambda}_h^{n-1}\|^2_{0,\Sigma}.\end{aligned}$$

The energy estimate (3.14) then follows my multiplying the previous expression by τ and then summing over $m = 1,\dots,n$, which completes the proof. ∎

4. Error estimate in a linearized setting. In this section, we provide an error analysis of Algorithm 3.1 in a simplified setting. To this purpose, we assume that the solid undergoes infinitesimal displacements and that convective effects are negligible in the fluid. Under these assumptions, the non-linear coupled problem (2.1)-(2.3) can be replaced by the following linear Stokes-elasticity system in the reference configuration $\Omega^{\mathrm{f}} \cup \Omega^{\mathrm{s}}$:

$$\begin{cases}\rho^{\mathrm{f}}\partial_t\boldsymbol{u} - \mathbf{div}\,\boldsymbol{\sigma}(\boldsymbol{u},p) = \boldsymbol{0} & \text{in} \quad \Omega^{\mathrm{f}}\times(0,T),\\ \mathrm{div}\,\boldsymbol{u} = 0 & \text{in} \quad \Omega^{\mathrm{f}}\times(0,T),\\ \boldsymbol{u} = \boldsymbol{0} & \text{on} \quad \Gamma^{\mathrm{f}}\times(0,T),\end{cases} \tag{4.1}$$

$$\begin{cases}\rho^{\mathrm{s}}\partial_t\dot{\boldsymbol{d}} - \mathbf{div}\,\boldsymbol{\sigma}(\boldsymbol{d}) = \boldsymbol{0} & \text{in} \quad \Omega^{\mathrm{s}}\times(0,T),\\ \dot{\boldsymbol{d}} = \partial_t\boldsymbol{d} & \text{in} \quad \Omega^{\mathrm{s}}\times(0,T),\\ \boldsymbol{d} = \boldsymbol{0} & \text{on} \quad \Gamma^{\mathrm{s}}\times(0,T),\end{cases} \tag{4.2}$$

$$\begin{cases}\boldsymbol{u} = \dot{\boldsymbol{d}} & \text{on} \quad \Sigma\times(0,T),\\ \boldsymbol{\sigma}(\boldsymbol{u},p)\boldsymbol{n} = \boldsymbol{\sigma}(\boldsymbol{d})\boldsymbol{n} & \text{on} \quad \Sigma\times(0,T),\end{cases} \tag{4.3}$$

complemented with the initial conditions: $\boldsymbol{d}(0,\cdot) = \boldsymbol{d}_0$, $\dot{\boldsymbol{d}}(0,\cdot) = \dot{\boldsymbol{d}}_0$ in Ω^{s}, and $\boldsymbol{u}(0,\cdot) = \boldsymbol{u}_0$ in Ω^{f} and where $T > 0$ denotes the final time. The symbol $\boldsymbol{\sigma}(\boldsymbol{d})$ stands for the linearized solid stress tensor, which is assumed to be given in terms of the solid displacement $\boldsymbol{d}$ by the following relation:

$$\boldsymbol{\sigma}(\boldsymbol{d}) \stackrel{\mathrm{def}}{=} 2L_1\boldsymbol{\epsilon}(\boldsymbol{d}) + L_2(\mathrm{div}\,\boldsymbol{d})\boldsymbol{I},$$

where $L_1, L_2 > 0$ denote the so called Lamé coefficients of the solid.

Assuming that $\boldsymbol{\lambda} \in L^2(\Sigma)$, the solution of (4.1)–(4.3) satisfies the weak formulation

$$
\begin{aligned}
\rho^{\mathrm{s}} \int_{\Omega^{\mathrm{s}}} \partial_t \dot{\boldsymbol{d}} \cdot \boldsymbol{\xi} + a^{\mathrm{s}}(\boldsymbol{d}, \boldsymbol{\xi}) + \int_{\Sigma} \boldsymbol{\lambda} \cdot \boldsymbol{\xi} &= 0, \\
\int_{\Omega^{\mathrm{s}}} \dot{\boldsymbol{d}} \cdot \boldsymbol{\phi} - \int_{\Omega^{\mathrm{s}}} \partial_t \boldsymbol{d} \cdot \boldsymbol{\phi} &= 0, \\
\rho^{\mathrm{f}} \int_{\Omega^{\mathrm{f}}} \partial_\tau \boldsymbol{u} \cdot \boldsymbol{v} + a^{\mathrm{f}}\big((\boldsymbol{u}, p), (\boldsymbol{v}, q)\big) - \int_{\Sigma} \boldsymbol{\lambda} \cdot \boldsymbol{v} &= 0, \\
\int_{\Sigma} (\boldsymbol{u} - \dot{\boldsymbol{d}}) \cdot \boldsymbol{\mu} &= 0
\end{aligned}
\tag{4.4}
$$

for all $(\boldsymbol{\xi}, \boldsymbol{\phi}, \boldsymbol{v}, q) \in \boldsymbol{V}^{\mathrm{s}} \times \boldsymbol{V}^{\mathrm{s}} \times \boldsymbol{V}^{\mathrm{f}} \times M^{\mathrm{f}}$. Here, the bilinear forms of the fluid, denoted as a^{f}, and of the solid, denoted as a^{s}, are respectively given by

$$
\begin{aligned}
a^{\mathrm{f}}\big((\boldsymbol{u}, p), (\boldsymbol{v}, q)\big) &\stackrel{\mathrm{def}}{=} 2\mu \int_{\Omega^{\mathrm{f}}} \boldsymbol{\epsilon}(\boldsymbol{u}) : \boldsymbol{\epsilon}(\boldsymbol{v}) - \int_{\Omega^{\mathrm{f}}} p \operatorname{div} \boldsymbol{v} + \int_{\Omega^{\mathrm{f}}} q \operatorname{div} \boldsymbol{u}, \\
a^{\mathrm{s}}\big(\boldsymbol{d}, \boldsymbol{\xi}\big) &\stackrel{\mathrm{def}}{=} 2L_1 \int_{\Omega^{\mathrm{s}}} \boldsymbol{\epsilon}(\boldsymbol{d}) : \boldsymbol{\epsilon}(\boldsymbol{\xi}) + L_2 \int_{\Omega^{\mathrm{s}}} (\operatorname{div} \boldsymbol{d})(\operatorname{div} \boldsymbol{\xi}).
\end{aligned}
$$

We also introduce the elastic energy norm of the solid given by the relation

$$
\|\boldsymbol{\xi}\|_{\mathrm{s}} \stackrel{\mathrm{def}}{=} \sqrt{a^{\mathrm{s}}\big(\boldsymbol{\xi}, \boldsymbol{\xi}\big)}
$$

for all $\boldsymbol{\xi} \in \boldsymbol{V}^{\mathrm{s}}$.

For the numerical approximation of (4.4) we consider the Robin-Robin loosely coupled scheme introduced in [6] and detailed in Algorithm 4.1. As in Section 3, we employ a backward Euler method for the fluid and a mid-point scheme for the solid. In addition, for the spatial discretization, we consider a piecewise affine continuous finite elements, where we assume that the fluid and solid meshes are fitted. In other words, Algorithm 4.1 is essentially the linear counterpart of Algorithm 3.1. Here, we accommodate for the lack of inf-sup stability by using a pressure stabilized bilinear form for the fluid (see [4]),

$$
a_h^{\mathrm{f}}\big((\boldsymbol{u}_h, p_h), (\boldsymbol{v}_h, q_h)\big) \stackrel{\mathrm{def}}{=} a^{\mathrm{f}}\big((\boldsymbol{u}_h, p_h), (\boldsymbol{v}_h, q_h)\big) + \frac{\gamma_{\mathrm{p}} h^2}{\mu} \int_{\Omega^{\mathrm{f}}} \boldsymbol{\nabla} p_h \cdot \boldsymbol{\nabla} q_h,
\tag{4.5}
$$

with $\gamma_{\mathrm{p}} > 0$ a user-defined parameter.

4.1. Relation to previous results. In [6], we proved that Algorithm 4.1 was optimal in space and sub-optimal in time, specifically $\mathcal{O}(h + \tau^{\frac{1}{2}})$. However, following new numerical experiments and the results of [7], it has become clear that the result in [6] is not a strict bound. Following the techniques developed in [7], we are able to prove that the Robin-Robin scheme for the linear case is, in fact, nearly-optimal in time. This result is presented below, along with the main features of the analysis. The full analysis is covered in detail in [13, Chapter 5].

4.2. Nearly-optimal error estimate. In what follows, $N \in \mathbb{N}$ is such that $N\tau \leqslant T$ and let $\big\{(\boldsymbol{u}_h^n, p_h^n, \boldsymbol{\lambda}_h^n, \boldsymbol{d}_h^n, \dot{\boldsymbol{d}}_h^n)\big\}_{1 \leqslant n \leqslant N} \subset \boldsymbol{V}_h^{\mathrm{f}} \times M_h^{\mathrm{f}} \times \boldsymbol{V}_h^{\mathrm{g}} \times \boldsymbol{V}_h^{\mathrm{s}} \times \boldsymbol{V}_h^{\mathrm{s}}$ be given by Algorithm 4.1. We introduce the discrete error terms

$$
\boldsymbol{e}_{\boldsymbol{d},h}^n \stackrel{\mathrm{def}}{=} \boldsymbol{d}_h^n - R_h^{\mathrm{s}} \boldsymbol{d}^n, \quad \boldsymbol{e}_{\dot{\boldsymbol{d}},h}^n \stackrel{\mathrm{def}}{=} \dot{\boldsymbol{d}}_h^n - R_h^{\mathrm{s}} \dot{\boldsymbol{d}}^n,
$$

Algorithm 4.1 Robin-based loosely coupled scheme (linear case).

Assume $\boldsymbol{u}_h^0$, $\boldsymbol{d}_h^0$ and $\boldsymbol{d}_h^{\mathrm{f},0}$, $\boldsymbol{\lambda}_h^0$ to be given and, for $n \geqslant 1$, perform:

1. Solid subproblem: Find $\dot{\boldsymbol{d}}_h^n, \boldsymbol{d}_h^n \in \boldsymbol{V}_h^{\mathrm{s}}$ such that $\dot{\boldsymbol{d}}_h^{n-\frac{1}{2}} = \partial_\tau \boldsymbol{d}_h^n$ and

$$\rho^{\mathrm{s}} \int_{\Omega^{\mathrm{s}}} \partial_\tau \dot{\boldsymbol{d}}_h^n \cdot \boldsymbol{\xi}_h + a^{\mathrm{s}}(\boldsymbol{d}_h^{n-\frac{1}{2}}, \boldsymbol{\xi}_h) + \alpha \int_\Sigma (\dot{\boldsymbol{d}}_h^{n-\frac{1}{2}} - \boldsymbol{u}_h^{n-1}) \cdot \boldsymbol{\xi}_h = -\int_\Sigma \boldsymbol{\lambda}_h^{n-1} \cdot \boldsymbol{\xi}_h \tag{4.6}$$

   for all $\boldsymbol{\xi}_h \in \boldsymbol{V}_h^{\mathrm{s}}$.
2. Fluid subproblem: Find $(\boldsymbol{u}_h^n, p_h^n) \in \boldsymbol{V}_h^{\mathrm{f}} \times M_h^{\mathrm{f}}$ such that

$$\rho^{\mathrm{f}} \int_{\Omega^{\mathrm{f}}} \partial_\tau \boldsymbol{u}_h^n \cdot \boldsymbol{v}_h + a_h^{\mathrm{f}}\big((\boldsymbol{u}_h^n, p_h^n), (\boldsymbol{v}_h, q_h)\big) + \alpha \int_\Sigma (\boldsymbol{u}_h^n - \dot{\boldsymbol{d}}_h^{n-\frac{1}{2}}) \cdot \boldsymbol{v}_h = \int_\Sigma \boldsymbol{\lambda}_h^{n-1} \cdot \boldsymbol{v}_h \tag{4.7}$$

   for all $(\boldsymbol{v}_h, q_h) \in \boldsymbol{V}_h^{\mathrm{f}} \times M_h^{\mathrm{f}}$.
3. Fluid-stress update: set $\boldsymbol{\lambda}_h^n \in \boldsymbol{V}_h^g$ as

$$\boldsymbol{\lambda}_h^n = \boldsymbol{\lambda}_h^{n-1} + \alpha(\dot{\boldsymbol{d}}_h^{n-\frac{1}{2}} - \boldsymbol{u}_h^n) \quad \text{on} \quad \Sigma. \tag{4.8}$$

$$\boldsymbol{e}_{\boldsymbol{u},h}^n \overset{\text{def}}{=} \boldsymbol{u}_h^n - R_h^{\mathrm{f}} \boldsymbol{u}^n, \quad e_{p,h}^n \overset{\text{def}}{=} p_h^n - S_h p^n, \quad \boldsymbol{e}_{\boldsymbol{\lambda},h}^n \overset{\text{def}}{=} \boldsymbol{\lambda}_h^n - \pi_h \boldsymbol{\lambda}^n,$$

where $\boldsymbol{\lambda}^n = \boldsymbol{\sigma}(\boldsymbol{u}^n, p^n)\boldsymbol{n}$ on the interface Σ and where R_h^{f}, R_h^{s} respectively denote the Scott-Zhang interpolants (see, e.g., [26]) projecting onto the finite element spaces $\boldsymbol{V}_h^{\mathrm{s}}$ and $\boldsymbol{V}_h^{\mathrm{f}}$, and S_h is the Scott-Zhang interpolant into M_h^{f} modified by a global constant so the average on Ω^{f} is zero. For projecting into $\boldsymbol{V}_h^{\mathrm{g}}$, we use the notation π_h, the L^2 orthogonal projection from $\boldsymbol{V}^{\mathrm{g}}$ to $\boldsymbol{V}_h^{\mathrm{g}}$. We employ the Scott-Zhang interpolant for this analysis because it allows significant flexibility when selecting the degrees of freedom. Indeed, we may choose the degrees of freedom so that we will have $R_h^{\mathrm{s}} \boldsymbol{v} = R_h^{\mathrm{f}} \boldsymbol{w}$ on Σ if $\boldsymbol{v} \in [H^1(\Omega^{\mathrm{s}})]^2$ and $\boldsymbol{w} \in [H^1(\Omega^{\mathrm{f}})]^2$ and $\boldsymbol{v} = \boldsymbol{w}$ on Σ.

We may then define the following quantities to construct our error estimate:

$$\mathcal{S}_h^n \overset{\text{def}}{=} \|\boldsymbol{e}_{\boldsymbol{d},h}^n\|_{\mathrm{s}}^2 + \rho^{\mathrm{s}} \|\boldsymbol{e}_{\dot{\boldsymbol{d}},h}^n\|_{0,\Omega^{\mathrm{s}}}^2 + \rho^{\mathrm{f}} \|\boldsymbol{e}_{\boldsymbol{u},h}^n\|_{0,\Omega^{\mathrm{f}}}^2,$$

$$\mathcal{E}_h^n \overset{\text{def}}{=} \tau\alpha \|\boldsymbol{e}_{\boldsymbol{u},h}^n\|_{0,\Sigma}^2 + \frac{\tau}{\alpha} \|\boldsymbol{e}_{\boldsymbol{\lambda},h}^n\|_{0,\Sigma}^2,$$

$$\mathcal{W}_h^n \overset{\text{def}}{=} \rho^{\mathrm{f}} \|\boldsymbol{e}_{\boldsymbol{u},h}^n - \boldsymbol{e}_{\boldsymbol{u},h}^{n-1}\|_{0,\Omega^{\mathrm{f}}}^2 + 4\mu\tau \|\boldsymbol{\varepsilon}(\boldsymbol{e}_{\boldsymbol{u},h}^n)\|_{0,\Omega^{\mathrm{f}}}^2 + 2\tau h^2 \|\nabla e_{p,h}^n\|_{0,\Omega^{\mathrm{s}}}^2,$$

$$\mathcal{Z}_h^n \overset{\text{def}}{=} \tau\alpha \|\boldsymbol{e}_{\dot{\boldsymbol{d}},h}^{n-\frac{1}{2}} - \boldsymbol{e}_{\boldsymbol{u},h}^{n-1}\|_{0,\Sigma}^2$$

for $1 \leqslant n \leqslant N$. Finally, as described in [13, Chapter 5], the quasi-optimal error result requires two key assumptions, which we state here. The motivation behind these assumptions will be explained further below. First, we assume that the normal $\boldsymbol{n}^{\mathrm{s}}$ can be extended from Σ into Ω^{s} in such a way that its gradient is bounded.

ASSUMPTION 1. *There exists* $\widetilde{\boldsymbol{n}}^{\mathrm{s}} \in [\mathbf{W}^{1,\infty}(\Omega^{\mathrm{s}})]^2$ *such that* $\widetilde{\boldsymbol{n}}^{\mathrm{s}}|_\Sigma = \boldsymbol{n}^{\mathrm{s}}$.

The second assumption is the existence of a function $\widetilde{\phi} : \Omega^{\mathrm{s}} \to \mathbb{R}$ that serves as a pseudo-lifting operator from the interface Σ into the interior of the solid domain Ω^{s}.

ASSUMPTION 2. *Assume that* $\tau < \frac{1}{2}$. *There exists a function* $\widetilde{\phi} : \Omega^{\mathrm{s}} \to \mathbb{R}$ *satisfying:*

(i) $0 \leqslant \widetilde{\phi} \leqslant 1$;
(ii) $\widetilde{\phi} \in \boldsymbol{V}^{\mathrm{s}}$;
(iii) $|\{x \in \Sigma : \widetilde{\phi}(x) \neq 1\}| \leqslant C\tau$;
(iv) $\left\|\boldsymbol{\nabla}\widetilde{\phi}\right\|^2_{0,\Omega^{\mathrm{s}}} \leqslant C\left(1+\log\frac{1}{\tau}\right)$;
where each $C>0$ represents a general constant independent of τ and of the physical parameters.

With these assumptions established, the quasi-optimal error results proceeds as follows.

THEOREM 2. *Under Assumptions 1 and 2, and assuming that the solution is smooth enough so that Y_h defined below and $\|\boldsymbol{\varepsilon}(\dot{\boldsymbol{d}})\|^2_{L^2(0,T;L^\infty(\Omega^{\mathrm{s}}))}$, $\|\operatorname{div}\dot{\boldsymbol{d}}\|^2_{L^2(0,T;L^\infty(\Omega^{\mathrm{s}}))}$ are bounded, we have the following bound on the discrete error*

$$\begin{aligned}(4.9)\quad &\max_{1\leqslant m\leqslant n}\left\{\mathcal{S}_h^m+\mathcal{E}_h^m\right\}+\sum_{m=1}^{n}\left(\mathcal{Z}_h^m+\mathcal{W}_h^m\right)\\ &\qquad\leqslant C\tau^2\Bigg[\frac{(1+T)(L_1+L_2)^3}{\alpha^2}\Big(\left(1+\log\tau^{-1}\right)\|\boldsymbol{\varepsilon}(\dot{\boldsymbol{d}})\|^2_{L^2(0,T;L^\infty(\Omega^{\mathrm{s}}))}\\ &\qquad\qquad+\|\operatorname{div}\dot{\boldsymbol{d}}\|^2_{L^2(0,T;L^\infty(\Omega^{\mathrm{s}}))}\Big)+Y_h\Bigg],\end{aligned}$$

where $Y_h \overset{\text{def}}{=} \sum_{i=1}^{3} Y_{i,h}$ is given by

$$\begin{aligned}Y_{1,h} \overset{\text{def}}{=} h^2\Bigg[&(1+h^2)\rho^{\mathrm{s}}(1+T)\|\partial_t\dot{\boldsymbol{d}}\|^2_{L^2(0,T;H^2(\Omega^{\mathrm{s}}))}+(1+h^2)\rho^{\mathrm{f}}T\|\partial_t\boldsymbol{u}\|^2_{L^2(0,T;H^2(\Omega^{\mathrm{f}}))}\\ &+(1+T)(L_1+L_2)\|\dot{\boldsymbol{d}}\|^2_{L^2(0,T;H^2(\Omega^{\mathrm{s}}))}+\mu\|\boldsymbol{u}\|^2_{L^2(0,T;H^2(\Omega^{\mathrm{f}}))}\\ &+\frac{h^2}{\mu}\|p\|^2_{L^2(0,T;H^2(\Omega^{\mathrm{f}}))}+(L_1+L_2)\|\boldsymbol{d}\|^2_{L^2(0,T;H^2(\Omega^{\mathrm{s}})}\\ &+(L_1+L_2)\|\boldsymbol{d}\|^2_{L^\infty(0,T;H^2(\Omega^{\mathrm{s}})}\Bigg]+\tau^2\Bigg[\tau^2\rho^{\mathrm{s}}(1+T)\|\partial_t{}^3\dot{\boldsymbol{d}}\|^2_{L^2(0,T;L^2(\Omega^{\mathrm{s}}))}\\ &+\rho^{\mathrm{f}}T\|\partial_t{}^2\boldsymbol{u}\|^2_{L^2(0,T;L^2(\Omega^{\mathrm{f}}))}+\frac{h^4}{\mu}\|\partial_t p\|^2_{L^2(0,T;H^2(\Omega^{\mathrm{f}}))}\\ &+h^2(L_1+L_2)\|\dot{\boldsymbol{d}}\|^2_{L^2(0,T;H^2(\Omega^{\mathrm{s}}))}+h^2\mu\|\partial_t\boldsymbol{u}\|^2_{L^2(0,T;H^2(\Omega^{\mathrm{f}}))}\Bigg],\end{aligned}$$

$$\begin{aligned}Y_{2,h} \overset{\text{def}}{=} \tau^2\Bigg[&(\tau^2)(1+T)(L_1+L_2)\|\partial_t^3\dot{\boldsymbol{d}}\|^2_{L^2(0,T;H^1(\Omega^{\mathrm{s}}))}+h^2\|\partial_t\boldsymbol{u}\|^2_{L^2(0,T;H^3(\Omega^{\mathrm{f}}))}\\ &+\left(1+\alpha+\frac{\alpha^2}{\mu}+\mu+\mu^2+\frac{(1+T)\mu^2}{\alpha}\right)\|\partial_t\boldsymbol{u}\|^2_{L^2(0,T;H^2(\Sigma))}\\ &+(1+\alpha)\|\partial_t\dot{\boldsymbol{d}}\|^2_{L^2(0,T;L^2(\Sigma)}+\left(1+\frac{1+T}{\alpha}+\frac{1}{\mu}\right)\|\partial_t p\|^2_{L^2(0,T;L^2(\Sigma))}\\ &+\tau^2(1+\alpha)\|\partial_t^3\dot{\boldsymbol{d}}\|^2_{L^2(0,T;L^2(\Sigma))}+T\rho^{\mathrm{s}}\|\partial_t^2\dot{\boldsymbol{d}}\|^2_{L^2(0,T;L^2(\Omega^{\mathrm{s}}))}\\ &+((1+T)(L_1+L_2)+\rho^{\mathrm{s}})\|\partial_t\dot{\boldsymbol{d}}\|^2_{L^2(0,T;H^1(\Omega^{\mathrm{s}}))}+\frac{\mu^2T}{\alpha}\|\boldsymbol{\varepsilon}(\partial_t\boldsymbol{u})\|^2_{L^2(0,T;L^\infty(\Sigma))}\end{aligned}$$

$$+\frac{T}{\alpha}\|\partial_t p\|^2_{L^2(0,T;L^\infty(\Sigma))}+\rho^{\mathrm{s}}\|\partial_t\dot{\boldsymbol{d}}\|^2_{L^\infty(0,T;L^2(\Omega^{\mathrm{s}}))}+h^2\|\partial_t p\|^2_{L^2(0,T;H^1(\Omega^{\mathrm{f}}))}\Big]$$

$$+h^2\big(\|\boldsymbol{u}\|^2_{L^2(0,T;H^3(\Omega^{\mathrm{f}}))}+\|\boldsymbol{\nabla} p\|^2_{L^2(0,T;L^2(\Omega^{\mathrm{f}}))}\big)$$

$$+h^4\left(\frac{T\mu^2}{\alpha}\|\partial_t\boldsymbol{u}\|^2_{L^2(0,T;H^2(\Sigma))}+\frac{T}{\alpha}\|\partial_t p\|^2_{L^2(0,T;H^1(\Sigma))}\right),$$

$$Y_{3,h}\overset{\text{def}}{=}\tau^2\Bigg[\frac{(1+T)(L_1+L_2)^3+\rho^{\mathrm{s}}(L_1^2+L_2^2)}{\alpha^2}\|\dot{\boldsymbol{d}}\|^2_{L^2(0,T;H^2(\Omega^{\mathrm{s}}))}$$

$$+\frac{\rho^{\mathrm{s}}T(L_1^2+L_2^2)}{\alpha^2}\|\partial_t\dot{\boldsymbol{d}}\|^2_{L^2(0,T;H^2(\Omega^{\mathrm{s}}))}+\frac{\rho^{\mathrm{s}}(L_1^2+L_2^2)}{\alpha^2}\|\dot{\boldsymbol{d}}\|^2_{L^\infty(0,T;H^1(\Omega^{\mathrm{s}}))}\Bigg].$$

4.3. Sketch of the proof to Theorem 2. The proof of Theorem 2 is only sketched below due to the page limit, we refer to [13, Theorem 5.2.9] for full details. The argument consists of three parts. First, we begin with a preliminary bound.

LEMMA 4.1. *For $1\leqslant n\leqslant N$, it holds*

$$\frac{3}{8}\max_{1\leqslant m\leqslant n}\left\{\mathcal{S}_h^m+\mathcal{E}_h^m\right\}+\frac{3}{8}\sum_{m=1}^{n}\left(\mathcal{W}_h^m+\mathcal{Z}_h^m\right)\leqslant\sum_{m=1}^{n}\frac{\tau}{\alpha}\int_\Sigma \boldsymbol{e}_{\lambda,h}^{m-1}\cdot\boldsymbol{g}_{3,h}^m+CD_h^n,$$

where

$$\boldsymbol{g}_{3,h}^n\overset{\text{def}}{=}\frac{\alpha}{2}\boldsymbol{g}_{1,h}^n+\pi_h\boldsymbol{g}_2^n,\quad \boldsymbol{g}_{1,h}^n\overset{\text{def}}{=}R_h^{\mathrm{f}}\boldsymbol{u}^n-R_h^{\mathrm{f}}\boldsymbol{u}^{n-1},\quad \boldsymbol{g}_2^n\overset{\text{def}}{=}\boldsymbol{\lambda}^n-\boldsymbol{\lambda}^{n-1}$$

and

$$D_h^n\overset{\text{def}}{=}\tau\sum_{m=1}^{n-1}\Bigg[\mu\|\boldsymbol{\varepsilon}((R_h^{\mathrm{f}}-I)\boldsymbol{u}^m)\|^2_{0,\Omega^{\mathrm{f}}}+\frac{1}{\mu}\|(S_h-I)p^m\|^2_{0,\Omega^{\mathrm{f}}}$$

$$+(1+T)\big\|R_h^{\mathrm{s}}\dot{\boldsymbol{d}}^{m-\frac{1}{2}}-\partial_\tau R_h^{\mathrm{s}}\boldsymbol{d}_h^n\big\|^2_{\mathrm{s}}+(1+T)\|(R_h^{\mathrm{s}}-I)\partial_\tau\boldsymbol{d}^m\|^2_{\mathrm{s}}+h^2\|\boldsymbol{u}^m\|^2_{H^3(\Omega^{\mathrm{f}})}$$

$$+(1+T)\big\|R_h^{\mathrm{s}}\dot{\boldsymbol{d}}^{m-\frac{1}{2}}-\partial_\tau R_h^{\mathrm{s}}\boldsymbol{d}_h^m\big\|^2_{\mathrm{s}}+(1+T)\|(R_h^{\mathrm{s}}-I)\partial_\tau\boldsymbol{d}^m\|^2_{\mathrm{s}}+h^2\|\boldsymbol{u}^m\|^2_{3,\Omega^{\mathrm{f}}}$$

$$+\left(\alpha+\frac{\alpha^2}{\mu}\right)\|\boldsymbol{g}_{1,h}^m\|^2_{0,\Sigma}+\left(1+\frac{1}{\alpha}+\frac{1}{\mu}\right)\|\boldsymbol{\lambda}^m-\boldsymbol{\lambda}^{m-1}\|^2_{0,\Sigma}$$

$$+T\rho^{\mathrm{s}}\|\partial_\tau R_h^{\mathrm{s}}\dot{\boldsymbol{d}}^m-\partial_t\dot{\boldsymbol{d}}^{m-\frac{1}{2}}\|^2_{0,\Omega^{\mathrm{s}}}+\rho^{\mathrm{f}}T\|\partial_\tau R_h^{\mathrm{f}}\boldsymbol{u}^m-\partial_t\boldsymbol{u}^m\|^2_{0,\Omega^{\mathrm{f}}}$$

$$+h^2\|\boldsymbol{\nabla} S_h p^m\|^2_{0,\Omega^{\mathrm{f}}}+\frac{\tau}{2\alpha}\|\boldsymbol{g}_{3,h}^m\|^2_{0,\Sigma}\Bigg]+\|(R_h^{\mathrm{s}}-I)\boldsymbol{d}^n\|^2_{\mathrm{s}}.$$

The proof of Lemma 4.1 requires some standard algebra along with Cauchy-Schwarz, Young's inequality, trace inequality, and Korn's inequality. A detailed proof is included in [13, Chapter 5]. The key takeaway, however, is that all of the terms in D_h^n are either the norms of splitting error terms such as $\boldsymbol{g}_{1,h}^n$ or interpolation errors such as $S_hp^n-p^n$. In both cases, the terms may be optimally bounded in terms of h and τ in the final step of the proof. However, the remaining unbounded term requires special care.

Consequently, the second part of the proof involves deriving a bound for the term

$$\sum_{m=1}^{n}\frac{\tau}{\alpha}\int_\Sigma \boldsymbol{e}_{\boldsymbol{\lambda},h}^{m-1}\cdot\boldsymbol{g}_{3,h}^m.$$

If we attempt to bound this term by balancing $\boldsymbol{e}_{\boldsymbol{\lambda},h}^{m-1}$ with terms appearing on the left-hand side of the estimate, we ultimately sacrifice a factor of $\tau^{\frac{1}{2}}$, resulting in suboptimal convergence, as done in [6]. Essentially, the challenge presented by this term is that it resides on the interface Σ, but to avoid a loss in accuracy we must somehow avoid the interface as much as possible.

To do this, we utilize the error equations of the solid to pull the term $\boldsymbol{e}_{\boldsymbol{\lambda},h}^{n-1}$ from the interface Σ into the interior domain Ω^{s}. However, this requires us to construct an extension of $\boldsymbol{g}_{3,h}^{n}$ into Ω^{s} which is in $\boldsymbol{V}_h^{\mathrm{s}}$. Critically, this means that the extension needs to vanish on $\partial\Omega^{\mathrm{s}}\backslash\Sigma$, which is not guaranteed for $\boldsymbol{g}_{3,h}^{n+1}$ due to the presence of the term $\pi_h(\boldsymbol{\lambda}^{n+1}-\boldsymbol{\lambda}^{n})$. Therefore, we will utilize the extended normal $\widetilde{\boldsymbol{n}}_s$ and the function $\widetilde{\phi}$ defined in Assumptions 1 and 2 to construct a cut-off function technique to continuously lift the residual $\boldsymbol{g}_{3,h}^{n+1}$ from $\boldsymbol{V}_h^{\mathrm{g}}$ into $\boldsymbol{V}_h^{\mathrm{s}}$.

The result of this extension step yields a quasi-optimal bound stated in the following lemma.

LEMMA 4.2. *Under Assumptions 1 and 2 we have*

$$\frac{\tau}{\alpha}\sum_{m=1}^{n}\int_{\Sigma}\boldsymbol{e}_{\boldsymbol{\lambda},h}^{m-1}\cdot\boldsymbol{g}_{3,h}^{m}\leqslant\frac{1}{8}\max_{1\leqslant m\leqslant n}\left\{\mathcal{S}_h^m+\mathcal{E}_h^m\right\}+\frac{1}{8}\sum_{m=1}^{n}\mathcal{Z}_h^m+C\Psi_h^n,$$

where $\Psi_h^n\overset{\text{def}}{=}\Psi_{1,h}^n+\Psi_{2,h}^n$ *given by*

$$\begin{aligned}
\Psi_1^n\overset{\text{def}}{=}&T\tau^3\rho^{\mathrm{s}}\sum_{m=1}^{n}\|{\partial_\tau}^2R_h^{\mathrm{s}}\dot{\boldsymbol{d}}^n\|_{0,\Omega^{\mathrm{s}}}^2+\rho^{\mathrm{s}}\|\boldsymbol{g}_{1,h}^n\|_{0,\Omega^{\mathrm{s}}}^2\\
&+\tau\sum_{m-1}^{m}\Bigg[(1+T)\|\boldsymbol{g}_{1,h}^m\|_{\mathrm{s}}^2+\big(1+\alpha\big)\|\boldsymbol{g}_{1,h}^m\|_{0,\Sigma}^2+\|\boldsymbol{\lambda}^m-\boldsymbol{\lambda}^{m-1}\|_{0,\Sigma}^2\\
&\qquad+\rho^{\mathrm{s}}\big\|\partial_\tau R_h^{\mathrm{s}}\dot{\boldsymbol{d}}^m-\partial_t\dot{\boldsymbol{d}}^{m-\frac{1}{2}}\big\|_{0,\Omega^{\mathrm{s}}}^2+\rho^{\mathrm{s}}\|\boldsymbol{g}_{1,h}^{n+1}\|_{0,\Omega^{\mathrm{s}}}^2+\|(R_h^{\mathrm{s}}-I)\boldsymbol{d}^{m-\frac{1}{2}}\|_{\mathrm{s}}^2\\
&\qquad+\alpha\|R_h^{\mathrm{f}}\boldsymbol{u}^m-\partial_\tau R_h^{\mathrm{s}}\boldsymbol{d}^m\|_{0,\Sigma}^2+\alpha\big\|R_h^{\mathrm{s}}\dot{\boldsymbol{d}}^{m-\frac{1}{2}}-\partial_\tau R_h^{\mathrm{s}}\boldsymbol{d}_h^m\big\|_{0,\Sigma}^2\Bigg],
\end{aligned}$$

$$\begin{aligned}
\Psi_2^n\overset{\text{def}}{=}&\frac{T\tau^3\rho^{\mathrm{s}}}{\alpha^2}\sum_{m=1}^{n}\big\|\partial_\tau^2R_h^{\mathrm{s}}\big(\widetilde{\phi}\boldsymbol{\sigma}(\boldsymbol{d}^{m-1})\widetilde{\boldsymbol{n}}^{\mathrm{s}}\big)\big\|_{0,\Omega^{\mathrm{s}}}^2+\frac{\rho^{\mathrm{s}}}{\alpha^2}\|\widetilde{\boldsymbol{g}}_{2,h}^n\|_{0,\Omega^{\mathrm{s}}}^2+\frac{Th^2}{\alpha}\sum_{m=1}^{n}\|\boldsymbol{g}_2^m\|_{1,\Sigma}^2\\
&+\tau\sum_{m=1}^{n}\Bigg[\frac{1+T}{\alpha^2}\|\widetilde{\boldsymbol{g}}_{2,h}^m\|_{\mathrm{s}}^2+\big(1+\frac{1}{\alpha}\big)\|\boldsymbol{\lambda}^{n+1}-\boldsymbol{\lambda}^n\|_{0,\Sigma}^2\\
&\qquad+\|\boldsymbol{g}_{1,h}^m\|_{0,\Sigma}^2+\rho^{\mathrm{s}}\|\partial_\tau R_h^{\mathrm{s}}\dot{\boldsymbol{d}}^m-\partial_t\dot{\boldsymbol{d}}^{m-\frac{1}{2}}\|_{0,\Omega^{\mathrm{s}}}^2+\frac{\rho^{\mathrm{s}}}{\alpha^2}\|\widetilde{\boldsymbol{g}}_{2,h}^m\|_{0,\Omega^{\mathrm{s}}}^2\\
&\qquad+\|(R_h^{\mathrm{s}}-I)\boldsymbol{d}^{m-\frac{1}{2}}\|_{\mathrm{s}}^2+\|R_h^{\mathrm{f}}\boldsymbol{u}^m-\partial_\tau R_h^{\mathrm{s}}\boldsymbol{d}^m\|_{0,\Sigma}^2\\
&\qquad+\big\|R_h^{\mathrm{s}}\dot{\boldsymbol{d}}^{m-\frac{1}{2}}-\partial_\tau R_h^{\mathrm{s}}\boldsymbol{d}_h^m\big\|_{0,\Sigma}^2+\frac{T}{\alpha}\|\boldsymbol{g}_2^m\|_{L^\infty(\Sigma)}^2\Bigg].
\end{aligned}$$

Finally, in the third step of the proof, it remains to bound the terms D_h^n and Ψ_h^n, which is the purpose of the next lemma.

LEMMA 4.3. *Under Assumptions 1 and 2, we have, for* $1\leqslant n\leqslant N$,

$$D_h^n + \Psi_h^n \leqslant C\tau^2 \left[\frac{(1+T)(L_1+L_2)^3}{\alpha^2} \Big(\big(1+\log\tau^{-1}\big) \|\boldsymbol{\varepsilon}(\dot{\boldsymbol{d}})\|^2_{L^2(0,T;L^\infty(\Omega^{\rm s}))} + \|\operatorname{div}\dot{\boldsymbol{d}}\|^2_{L^2(0,T;L^\infty(\Omega^{\rm s}))} \Big) + CY_h \right].$$

The error estimate (4.9) then follows by combining the results of Lemmas 4.1–4.3.

5. Numerical examples. In this section, we illustrate the accuracy properties of Algorithms 3.1 in a series of well-known numerical examples.

5.1. Convergence study in a simplified framework. The objective of this first example is to provide numerical evidence of the nearly-optimal convergence result of Theorem 2. We will in particular investigate the effect on the accuracy of the solid parameters L_1, L_2 involved in the error estimate (4.9). To this purpose, we consider the pressure wave propagation benchmark of [18, Section 6.1.1] with the simplified coupled problem (4.1)-(4.3). We hence take $\Omega^{\rm f} = [0,L]\times[0,R]$, $\Omega^{\rm s} = [0,L]\times[R,R+\epsilon]$, with $L = 6$, $R = 0.5$ and $\epsilon = 0.1$. All the units are in the CGS system. At the fluid inlet boundary $x = 0$ a sinusoidal pressure of maximal amplitude $2\cdot 10^4$ is enforced during $5\cdot 10^{-3}$ second. Zero traction is prescribed at the oulet $x = 6$ and a symmetry condition is enforced on the lower wall. Transverse membrane effects are included in the solid equation $(4.2)_1$ through the additional zeroth-order term $c_0\boldsymbol{d}$. The solid is clamped at its extremities and zero traction is enforced on its top boundary.

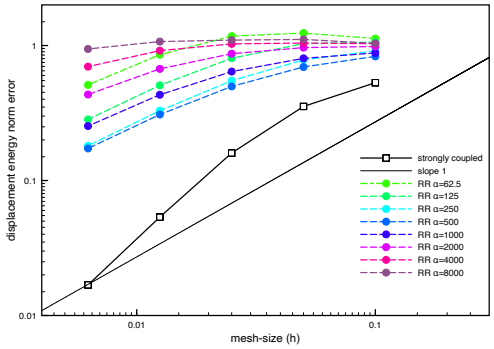

FIG. 1. *Convergence histories for* $E = 1.58\cdot 10^6$.

The fluid and solid physical parameters are $\rho^{\rm f} = 1$, $\mu = 0.035$, $\rho^{\rm s} = 1.1$, $L_1 = 1.15\cdot 10^6$, $L_2 = 1.7\cdot 10^6$ and $c_0 = 4\cdot 10^6$. The pressure stabilization parameter in (4.5) is set to $\gamma_{\rm p} = 10^{-3}$. All the computations have been carried out with the `FreeFem++` software (see [25]).

In order to illustrate the accuracy of Algorithm 4.1, we evaluate the relative displacement error $\|\boldsymbol{d}_h^N - \boldsymbol{d}(T)\|_{\rm e} / \|\boldsymbol{d}(T)\|_{\rm e}$ at the final time $T = 0.015$ for different values of the discretization parameters under $\tau = \mathcal{O}(h)$, namely,

$$\tau \in \{5\cdot 10^{-4}/2^i\}_{i=0}^4, \quad h \in \{0.1/2^i\}_{i=0}^4.$$

The relative errors are calculated with a reference solution obtained with an implicit coupling scheme and a fine space-time grid ($h = 0.003125$ and $\tau = 10^{-6}$). The resulting convergence histories are reported in Figures 1–3 for three decreasing values

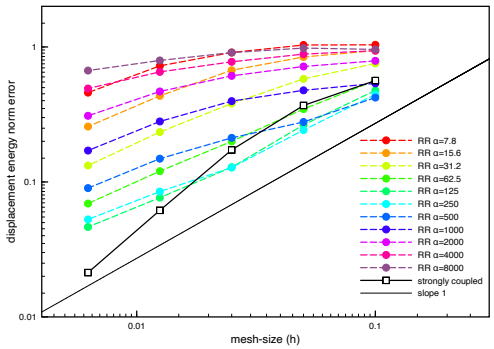

FIG. 2. *Convergence histories for* $E = 3.16 \cdot 10^5$.

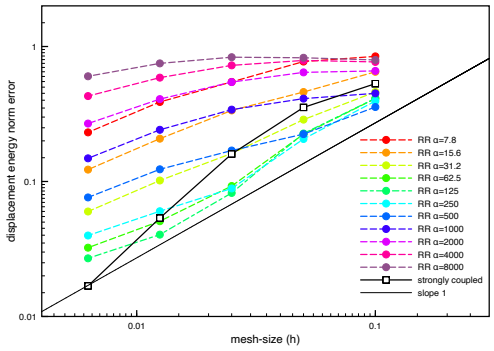

FIG. 3. *Convergence histories for* $E = 1.58 \cdot 10^5$.

of the Young modulus E. For comparison purposes, the results obtained with the implicit coupling scheme are also provided.

Several remarks are in order. The results indicate that there exists an optimal value of the Robin parameter α in terms of accuracy, and that accuracy tends to degrade for large or small values of α. Figures 1–3 also show that overall first-order accuracy $\mathcal{O}(h)$ is obtained for some values of α. This is more noticeable in Figures 2 and 3. The results show that accuracy tends to degrade when increasing the elastic parameters L_1 and L_2. All these observations are in agreement with the error estimate provided by Theorem 2. The results of Figures 1–3 indicate also that the optimal value of the Robin parameter α is proportional to $\sqrt{E}$. Such scaling equilibrates the contributions of the error bound provided by Theorem 2, which suggests the choice $\alpha = \gamma\sqrt{\rho^{\mathrm{s}} E}$, with γ a user-defined dimensionless parameter.

5.2. Lid-driven cavity with flexible bottom. As second numerical example, we consider the classical shear-driven cavity problem with a flexible bottom (see, e.g., [20]). The fluid domain is the unit square $\Omega^{\mathrm{f}} = [0,1] \times [0,1]$ with the fluid-solid interface on the lower boundary $\Sigma = [0,1] \times \{0\}$. All the units are given in the SI system.

The system is described by the non-linear coupled problem (2.1)-(2.3) in which the solid model (2.2) is replaced by a non-linear Timoshenko beam (see, e.g., [3]). The overall system is initially at rest and an oscillating shear velocity profile is imposed on the upper boundary $\boldsymbol{u}(t) = (1 - \cos(0.4\pi t), 0)^{\mathrm{T}}$ on $[0,1] \times \{1\}$. A no-slip condition is

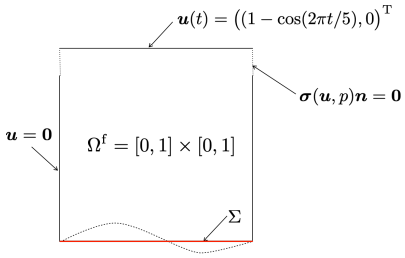

FIG. 4. *Geometric description.*

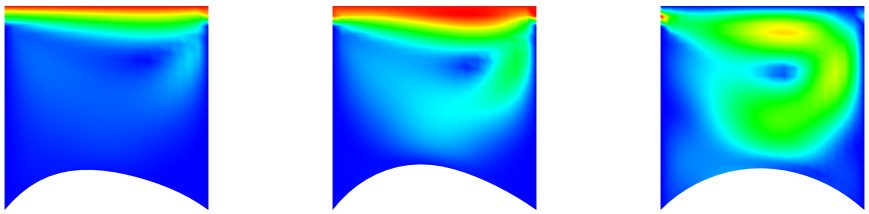

(a) $t = 2.8 \cdot 10^{-2}$ (b) $t = 2.9 \cdot 10^{-2}$ (c) $t = 3.0 \cdot 10^{-2}$

FIG. 5. *Snapshots of the fluid velocity in the deformed configuration at three different time instants obtained with Algorithm 3.1 and* $\alpha = 1$.

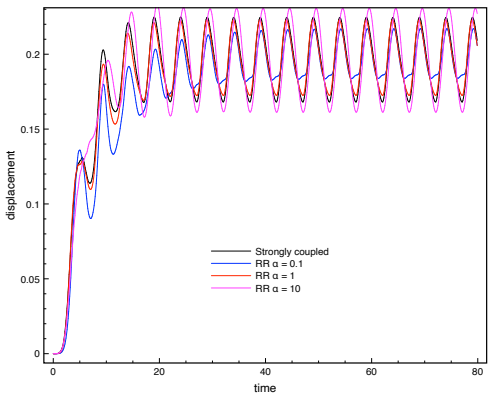

FIG. 6. *Time history of the mid-point displacement magnitude obtained with Algorithm 3.1, for three different values of* α*, and a strongly coupled scheme.*

enforced on the portions $\{0,1\}\times[0,0.9]$ of the lateral cavity walls, and zero traction is prescribed on theremaining parts $\{0,1\}\times[0.9,1]$. The fluid physical parameters are given by $\rho^{\mathrm{f}} = 1.0$ and $\mu = 0.01$, and for the solid $\rho^{\mathrm{s}} = 250$, $\epsilon = 0.002$, $E = 250$ and $\nu = 0$.

The spatial fluid approximation in (3.11) is made of $\mathbb{Q}_1/\mathbb{Q}_1$ finite elements with a SUPG/PSPG stabilized formulation. Linear MITC beam elements are used for the approximation of the Timoshenko beam in (3.10). In this numerical example, the computational meshes for the fluid and the solid meshes are, respectively, made of 400 quadrilaterals and of 20 segments and a time-step length of $\tau = 0.1$ is considered.

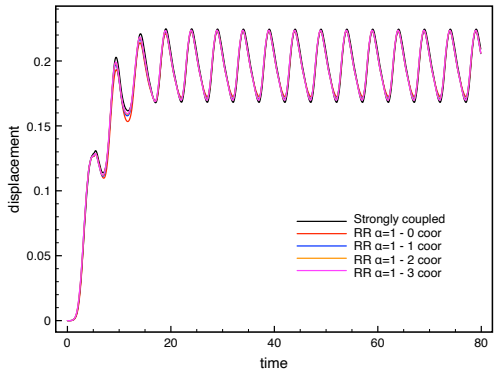

FIG. 7. *Time history of the interface mid-point displacement magnitude obtained with Algorithm 3.1, for $\alpha = 1$ and different correction iterations, and a strongly coupled scheme.*

All the numerical computations have been performed with the `FELiScE` library[1].

For illustration purposes, we have reported in Figure 5 some snapshots of the fluid velocity magnitude in the current configuration at different time-instants, obtained with Algorithm 3.1 and $\alpha = 1$. We now focus on the accuracy of this loosely coupled scheme. To this purpose, we have first reported in Figure 6 the magnitude of the interfacial mid-point displacement obtained with Algorithm 3.1, for different values of α, and with a strongly coupled scheme. The impact of α on the accuracy is clearly visible. As in the previous numerical example (Section 5.1), the accuracy of Algorithm 3.1 degrades when α is both smaller and larger than the optimal value (here, around $\alpha = 1$). It is also worth noting the very good accuracy of the results obtained with Algorithm 3.1 and $\alpha = 1$. Indeed, without any correction iteration the proposed loosely coupled scheme delivers practically the same accuracy as the strongly coupled scheme. This observation is in line with the results of the previous section (Figures 1–3) and the error estimate of Theorem 2, which indicate that small values of the solid elastic parameters yield a low splitting error.

Finally, Figure 7 compares the results obtained with Algorithm 3.1 for $\alpha = 1$ and different correction iterations. We recall that one correction iteration corresponds to performing once more steps (3.10), (3.11) and (3.12) of Algorithm 3.1 with updated Robin conditions, that is, by initializing $\boldsymbol{\lambda}^{n-1}$ and $\widehat{\boldsymbol{u}}^{n-1}|_\Sigma$ with the last values of $\boldsymbol{\lambda}^n$ and $\widehat{\boldsymbol{u}}^n|_\Sigma$. Since the accuracy is already very good without any correction, it only slight improves as we increase the number of corrections.

5.3. Pressure wave in an elastic tube. We consider the 3D non-linear counterpart of the numerical example considered in Section 5.1, viz., the propagation of a pressure wave within an elastic tube (see, e.g., [19, Chapter 12]). The fluid domain is a straight tube of radius 0.5 and length 5. The vessel wall has a thickness of 0.1. All the units are given in the CGS system. The fluid-structure system is modeled by the non-linear coupled problem (2.1)-(2.3). The overall system is initially at rest and an over pressure of $1.3332 \cdot 10^4$ is imposed on the inlet boundary during the time interval $[0, 0.005]$. The solid wall is clamped at its extremities. The physical parameters for the fluid are $\rho^{\mathrm{f}} = 1$ and $\mu = 0.035$, and for the solid $\rho^{\mathrm{s}} = 1.2$, $E = 3 \cdot 10^6$ and $\nu = 0.3$. In (3.10) and (3.11) continuous $\mathbb{P}_1$ finite elements are used (a SUPG/PSPG stabilized formulation is considered in the fluid). All the numerical computations have been

[1] https://gitlab.inria.fr/felisce/felisce

performed with the `FELiScE` library.

To highlight the fluid-structure interaction in this numerical example, Figure 8 shows snapshots of the fluid pressure in the deformed configuration at different time-instants, obtained using Algorithm 3.1 with $\alpha = 500$. We will now assess the influence

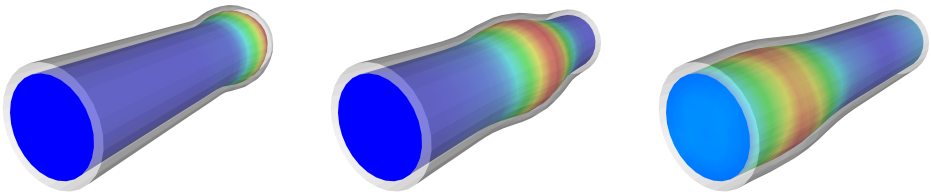

(a) $t = 3 \cdot 10^{-3}$ (b) $t = 7 \cdot 10^{-3}$ (c) $t = 1.2 \cdot 10^{-2}$

FIG. 8. *Snapshots of the fluid pressure in the deformed configuration at three different time instants with* $\alpha = 500$.

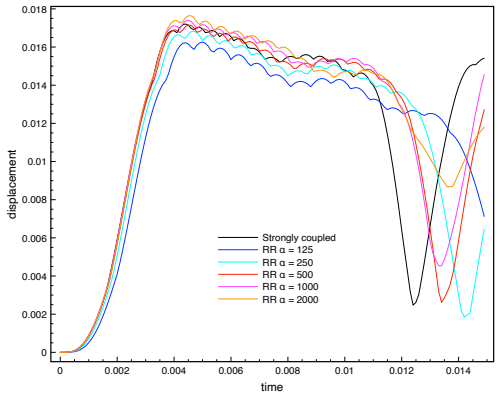

FIG. 9. *Time history of the interface mid-point displacement magnitudes with implicit coupling and RR algorithm with different* α.

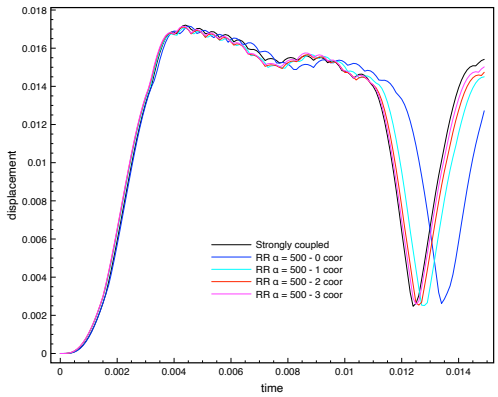

FIG. 10. *Time history of the interface mid-point displacement magnitudes with implicit coupling and RR algorithm with* $\alpha = 500$ *and different corrections.*

of the parameter α. In Figure 9, we display the magnitude of the interfacial mid-point displacement calculated using Algorithm 3.1 for various α values. These results are then compared to those obtained using a strongly coupled scheme. As observed in the previous numerical examples, the performance of Algorithm 3.1 is closely linked to the choice of α. Specifically, Algorithm 3.1 shows good accuracy when α is approximately 500. However, as we deviate from this range, both smaller and larger values of α tend to degrade the accuracy.

Figure 10 illustrates the impact of some correction iterations in Algorithm 3.1 with $\alpha = 500$. We observe an improvement in the accuracy of Algorithm 3.1 as we increase the number of corrections. It is worth noting that a single iteration significantly improves the accuracy. Large values of the solid physical parameters can negatively impact the solution, necessitating correction iterations to achieve accurate results.

6. Conclusion. We have extended the stability results of the loosely coupled Robin-Robin coupling from [6] to the fully nonlinear case. A nearly-optimal error estimate was also reported for the linear case. The numerical section validated the theoretical results, but also pointed to the importance of making a judicious choice of the Robin parameter α in order to observe optimal convergence in the range of discretization parameters used.

REFERENCES

[1] S. Badia, F. Nobile, and C. Vergara, *Robin-Robin preconditioned Krylov methods for fluid-structure interaction problems*, Comput. Methods Appl. Mech. Engrg., 198 (2009), pp. 2768–2784, https://doi.org/10.1016/j.cma.2009.04.004, https://doi.org/10.1016/j.cma.2009.04.004.

[2] J. W. Banks, W. D. Henshaw, and D. W. Schwendeman, *An analysis of a new stable partitioned algorithm for FSI problems. Part I: Incompressible flow and elastic solids*, J. Comput. Phys., 269 (2014), pp. 108–137, https://doi.org/10.1016/j.jcp.2014.03.006, https://doi.org/10.1016/j.jcp.2014.03.006.

[3] K. Bathe, *Finite Element Procedures*, Prentice Hall, 1996.

[4] F. Brezzi and J. Pitkäranta, *On the stabilization of finite element approximations of the Stokes equations*, in Efficient solutions of elliptic systems (Kiel, 1984), vol. 10 of Notes Numer. Fluid Mech., Vieweg, 1984, pp. 11–19.

[5] M. Bukač, S. Čanić, R. Glowinski, B. Muha, and A. Quaini, *A modular, operator-splitting scheme for fluid-structure interaction problems with thick structures*, Internat. J. Numer. Methods Fluids, 74 (2014), pp. 577–604, https://doi.org/10.1002/fld.3863, https://doi.org/10.1002/fld.3863.

[6] E. Burman, R. Durst, M. Fernández, and J. Guzmán, *Fully discrete loosely coupled Robin-Robin scheme for incompressible fluid-structure interaction: stability and error analysis*, Numer. Math., 151 (2022), pp. 807–840, https://doi.org/10.1007/s00211-022-01295-y, https://doi.org/10.1007/s00211-022-01295-y.

[7] E. Burman, R. Durst, M. Fernández, and J. Guzmán, *Loosely coupled, non-iterative time-splitting scheme based on Robin-Robin coupling: unified analysis for parabolic/parabolic and parabolic/hyperbolic problems*, J. Numer. Math., 31 (2023), pp. 59–77, https://doi.org/10.1515/jnma-2021-0119, https://doi.org/10.1515/jnma-2021-0119.

[8] E. Burman, R. Durst, and J. Guzmán, *Stability and error analysis of a splitting method using Robin-Robin coupling applied to a fluid-structure interaction problem*, Numer. Methods Partial Differential Equations, 38 (2022), pp. 1396–1406, https://doi.org/10.1002/num.22840, https://doi.org/10.1002/num.22840.

[9] E. Burman and M. Fernández, *Stabilization of explicit coupling in fluid-structure interaction involving fluid incompressibility*, Comput. Methods Appl. Mech. Engrg., 198 (2009), pp. 766–784, https://doi.org/10.1016/j.cma.2008.10.012, https://doi.org/10.1016/j.cma.2008.10.012.

[10] E. Burman and M. Fernández, *Explicit strategies for incompressible fluid-structure interaction problems: Nitsche type mortaring versus Robin-Robin coupling*, Internat. J. Nu-

mer. Methods Engrg., 97 (2014), pp. 739–758, https://doi.org/10.1002/nme.4607, https://doi.org/10.1002/nme.4607.

[11] E. Burman, M. Fernández, and P. Hansbo, *Continuous interior penalty finite element method for Oseen's equations*, SIAM J. Numer. Anal., 44 (2006), pp. 1248–1274.

[12] P. Causin, J. F. Gerbeau, and F. Nobile, *Added-mass effect in the design of partitioned algorithms for fluid-structure problems*, Comput. Methods Appl. Mech. Engrg., 194 (2005), pp. 4506–4527, https://doi.org/10.1016/j.cma.2004.12.005, https://doi.org/10.1016/j.cma.2004.12.005.

[13] R. Durst, *Recent Advances in Splitting Methods Based on Robin-Robin Coupling Conditions*, PhD thesis, Brown University, 2022, https://repository.library.brown.edu/studio/item/bdr:v34deskr/.

[14] C. Farhat, P. Geuzaine, and C. Grandmont, *The discrete geometric conservation law and the nonlinear stability of ale schemes for the solution of flow problems on moving grids*, Journal of Computational Physics, 174 (2001), pp. 669–694.

[15] C. Farhat, M. Lesoinne, and P. LeTallec, *Load and motion transfer algorithms for fluid/structure interaction problems with non-matching discrete interfaces: momentum and energy conservation, optimal discretization and application to aeroelasticity*, Comput. Methods Appl. Mech. Engrg., 157 (1998), pp. 95–114, https://doi.org/10.1016/S0045-7825(97)00216-8, https://doi.org/10.1016/S0045-7825(97)00216-8.

[16] M. Fernández and J.-F. Gerbeau, *Algorithms for fluid-structure interaction problems*, in Cardiovascular mathematics, vol. 1 of MS&A. Model. Simul. Appl., Springer, 2009, pp. 307–346.

[17] M. Fernández and J. Mullaert, *Convergence and error analysis for a class of splitting schemes in incompressible fluid-structure interaction*, IMA J. Numer. Anal., 36 (2016), pp. 1748–1782, https://doi.org/10.1093/imanum/drv055, https://doi.org/10.1093/imanum/drv055.

[18] M. Fernández, J. Mullaert, and M. Vidrascu, *Generalized Robin-Neumann explicit coupling schemes for incompressible fluid-structure interaction: stability analysis and numerics*, Internat. J. Numer. Methods Engrg., 101 (2015), pp. 199–229.

[19] L. Formaggia, A. Quarteroni, and A. Veneziani, eds., *Cardiovascular Mathematics. Modeling and simulation of the circulatory system*, vol. 1 of Modeling, Simulation and Applications, Springer, 2009.

[20] C. Förster, W. Wall, and E. Ramm, *Artificial added mass instabilities in sequential staggered coupling of nonlinear structures and incompressible viscous flows*, Comput. Methods Appl. Mech. Engrg., 196 (2007), pp. 1278–1293.

[21] G. Gigante and C. Vergara, *On the stability of a loosely-coupled scheme based on a Robin interface condition for fluid-structure interaction*, Comput. Math. Appl., 96 (2021), pp. 109–119, https://doi.org/10.1016/j.camwa.2021.05.012, https://doi.org/10.1016/j.camwa.2021.05.012.

[22] G. Gigante and C. Vergara, *On the stability of a loosely-coupled scheme based on a Robin interface condition for fluid-structure interaction*, Comput. Math. Appl., 96 (2021), pp. 109–119, https://doi.org/10.1016/j.camwa.2021.05.012, https://doi.org/10.1016/j.camwa.2021.05.012.

[23] O. Gonzalez, *Exact energy and momentum conserving algorithms for general models in nonlinear elasticity*, Computer Methods in Applied Mechanics and Engineering, 190 (2000), pp. 1763–1783.

[24] P. Hansbo, J. Hermansson, and T. Svedberg, *Nitsche's method combined with space-time finite elements for ALE fluid-structure interaction problems*, Comput. Methods Appl. Mech. Engrg., 193 (2004), pp. 4195–4206, https://doi.org/10.1016/j.cma.2003.09.029, https://doi.org/10.1016/j.cma.2003.09.029.

[25] F. Hecht, *New development in FreeFem++*, J. Numer. Math., 20 (2012), pp. 251–265.

[26] L. Scott and S. Zhang, *Finite element interpolation of nonsmooth functions satisfying boundary conditions*, Mathematics of Computation, 54 (1990), pp. 483–493.

[27] A. Seboldt and M. Bukač, *A non-iterative domain decomposition method for the interaction between a fluid and a thick structure*, Numer. Methods Partial Differential Equations, 37 (2021), pp. 2803–2832.

[28] S. Smaldone, *Numerical analysis and simulations of coupled problems for the cardiovascular system*, PhD thesis, Université Pierre et Marie Curie, 2014. https://tel.archives-ouvertes.fr/tel-01287506.

[29] T. Tezduyar, *Stabilized finite element formulations for incompressible flow computations*, vol. 28 of Advances in Applied Mechanics, Elsevier, 1991, pp. 1–44, https://doi.org/https://doi.org/10.1016/S0065-2156(08)70153-4.